https://dx.doi.org/10.1016/j.matchar.2024.113780

Delving into the intrinsic co-relation between microstructure and mechanical behaviour of fine-/ultrafine-grained TWIP steels via TEM and in-situ EBSD observation

Wang Cai[a,b,d], Chaoyang Sun[a,b,*], Hongjia Zhang[c], Chunhui Wang[a,b], Linghui Meng[a,b], M.W. Fu[d,#]

[a] School of Mechanical Engineering, University of Science and Technology Beijing, Beijing 100083, China

[b] Beijing Key Laboratory of Lightweight Metal Forming, Beijing 100083, China

[c] Vibration and Acoustics Research Group, Laboratory of Science and Technology on Integrated Logistics Support, College of Intelligence Science and Technology, National University of Defense Technology, Changsha 410073, China

[d] Department of Mechanical Engineering, Research Institute for Advanced Manufacturing, The Hong Kong Polytechnic University, Hung Hom, Kowloon, Hong Kong, China

Abstract

To illustrate the microstructural factors of grain refinement for enhancing mechanical properties, the fine-/ultrafine-grained TWIP steels with a product of strength and elongation of ~71 GPa·% were first prepared by combining rolling and stress relief annealing. Subsequently, the evolution of dislocations, stacking faults, and associated substructures of the fine-/ultrafine-grained TWIP steels was analysed by using in-situ EBSD tensile tests and TEM characterisation of the interrupted strain experiments. The results reveal that the excellent mechanical properties of the TWIP steels are attributed to dislocations and associated dislocation cells, dislocation walls, dislocation tangles, stacking faults and associated Lomer-Cottrell locks (LCs), nano-twins, primary and secondary twins and their interactions during plastic deformation. The density of geometrically necessary dislocations (GNDs) was evaluated based on the modified

Ashby′s model and compared with experimental results, indicating that grain size heterogeneity can promote the accumulation of GNDs, which facilitates the generation of subgrains and new boundaries to reduce the mean free path (MFP) of dislocations, thus enhancing strain hardening. Meanwhile, the interaction of lamellar primary and secondary twins in fine grains and the generation of stacking faults and nano-twins in ultrafine grains at higher strains can further promote strain hardening to elevate strength. Furthermore, the effects of grain orientation and grain size on the activation and evolution of dislocations and twins were elucidated. In ultrafine grains, twinning is strongly inhibited due to the elevated critical shear stress for twinning, resulting in more stacking faults and nano-twins, but fewer dislocation cells. The present work contributes to an in-depth understanding of the mechanical properties of fine-/ultrafine-grained materials to exploit their potential for industrial applications.

Keywords: Fine and ultrafine grains; Nano-twin; Mechanical behaviour; In-situ EBSD; TWIP steels.

*,# Corresponding authors: Chaoyang Sun, M.W. Fu

E–mail: suncy@ustb.edu.cn (Chaoyang Sun), mmmwfu@polyu.edu.hk (M.W. Fu)

1. Introduction

Twinning-induced plasticity (TWIP) steels have been a research hotspot over the last decade due to the perfect combination of high strength (>1 GPa) and considerable plasticity (>60%) [1]. The excellent mechanical properties are attributed to the abundant deformation twins and dislocations that can provide continuous strain hardening during plastic deformation, making them a promising candidate for large-scale applications in the automotive and structural industries [2]. Unfortunately, the relatively low yield strength (YS: 200-500 MPa) of TWIP steels compared to the advanced high strength steels (AHSSs) greatly limits their wide application in industries [3]. Therefore, grain refinement strategies such as severe plastic deformation (SPD), including equal channel angular pressing (ECAP) [4-6], surface mechanical attrition treatment (SMAT) [7], high pressure torsion (HPT) [8], and accumulative roll-bonding (ARB) [9, 10], have been employed to improve the YS of TWIP steels in recent years [2]. However, there is often a trade-off between strength and ductility in these strategies [11]. In particular, plasticity loss after grain refinement to fine and ultrafine grains (100 nm<d<1 μm) [12, 13] is a technological bottleneck in enhancing mechanical properties [14-16]. In order to develop new approaches to address the simultaneous enhancement of strength and ductility, it is urgent to further elucidate the activation and evolution of the plastic deformation mechanisms affecting the mechanical behaviour of fine-/ultrafine-grained TWIP steels.

It is widely accepted that the excellent mechanical properties of TWIP steels with moderate stacking fault energy (SFE), typically in 18-45 mJ/m^2 [17] or 20-40 mJ/m^2 [18], are mainly attributed to the dynamic interaction between deformation twins and dislocations during plastic deformation [19, 20]. The abundant deformation twins in the grains reduce the mean free path (MFP) of dislocations [21], which increases the chance that the motion of mobile dislocations is blocked by boundaries to enhance strain hardening [22], while the layered structure of twins induces an increase in dislocation back stresses, which further enhances strain hardening

capacity [22]. Meanwhile, as the grain size decreases, the evolution of stress induced by the blocked dislocations near grain boundaries (GBs) can be approximated as a linear increase in YS of polycrystalline materials with decreasing square root of the grain size, i.e., the Hall-Petch effect [23]. On the other hand, grain refinement increases the critical resolved shear stress (CRSS) for twinning and thus retards mechanical twinning [2, 24], called the reverse grain size effect of twin [25], which is related to the combined effect of the SFE and grain size [25]. Grain refinement is thought to increase the SFE [15], while higher SFE inhibits deformation twinning and facilitates dislocation slip [26]. Therefore, the effect of grain refinement on the competition and synergy of dislocation slip and deformation twinning needs to be further explored.

Twins typically nucleate near GBs during plastic deformation of TWIP steels and serve as a barrier to dislocation slip resulting in dynamic grain refinement, i.e., called the dynamic Hall-Petch effect [19, 27]. Indeed, the nucleation of twins and the subsequent development of twin substructures were also regulated and controlled by grain size [28]. For example, the frequency of deformation twins decreased when the average grain size was reduced to 3 μm [24]. This was consistent with the conclusion that the number of in-grain deformation twins also decreased significantly when the average grain size was reduced to 1.8 μm, indicating that deformation twinning was strongly inhibited by grain refinement [29]. However, it was recently found that grain refinement increased the number density of deformation twin nucleation near GBs when the grain size was less than 1 μm, even though deformation twinning was suppressed [30]. Furthermore, it was reported that the dominant mode of initial plastic deformation changed from dislocation slip and tangle to stacking faults in Fe-22Mn-0.6C TWIP steel grains less than or equal to 1 μm [2], which was also confirmed by the result that ultrafine-grained Fe-31Mn3Al-3Si austenitic TWIP steel was observed at yielding [14]. These TWIP steels in these experiments usually contain both fine and ultrafine grains [2, 14, 31], which may be more favourable for comparing the activation and evolution of slip and twinning close proximity to

critical size grains [14]. Whether grain refinement inhibits or enhances deformation twin nucleation needs to be determined experimentally via tracing the microstructural evolution and mechanical behaviour from initial plastic deformation to fracture [32] to elucidate the grain size dependence of the twin nucleation and growth.

The activation of slip and twinning is not only influenced by the grain size [29, 33], but also by the grain orientation, the local stress state and the mechanical behaviour of the neighbouring grains, for instance, twin bundles in neighbouring grains [24]. It is confident that the activation of slip and twinning is directly regulated by the maximum shear stress for slip and twinning [2]. The suppression of mechanical twinning was regarded as similar to the suppression of ε-martensite formation by grain refinement, whereby mechanical twinning might be delayed by an increase in the SFE of the C-atom segregation near the GBs or the dislocation back stress [34, 35], which was achieved by elevating the CRSS for twinning in TWIP steels [24, 25]. In turn, dislocation activation was also controlled by grain size, as illustrated by the observation of planar slip and cross-slip of dislocations via the in-situ transmission electron microscopy (TEM) test, which elaborated the role of dislocation activity in influencing the plastic deformation [36]. Indeed, the inhibition of twinning might be due to the rapid accumulation of dislocations resulting in an increase in the back stress of the dislocations on the slip plane, whereas the high level of back stress narrowed the width of the stacking faults, promoted cross-slip of the dislocations, and reduced the interaction of partial dislocations required for mechanical twinning [33]. Meanwhile, most of the stacking faults and deformation twins in ultrafine grains were associated with GBs, and thus the synergy and competition between slip and twinning were closely related to GBs [2]. When the grains were smaller than the critical size, GBs became the main sources and sinks of dislocations [37]. During tensile deformation, the grains gradually rotated with increasing strain. Meanwhile, the lattice rotation paths and rates were highly heterogeneous both between grains and in individual

grains, contributing to the formation of subgrains [38], which promoted the generation of new boundaries and varied the GBs fraction, resulting in a dynamic variation of grain size which further influenced the competition and synergies of slip and twinning.

To further decipher the intrinsic relationship between microstructure and mechanical properties, a micromechanical tensile experimental method is utilized for in-situ EBSD observation of fine-/ultrafine-grained TWIP steels prepared by rolling and stress relief annealing in this work. Simultaneously, the activation and evolution of dislocations, stacking faults, dislocation substructures, stacking fault substructures and their interactions, are explored based on interrupted strain experiments and TEM characterisation to elucidate the effect of different deformation mechanisms on strain hardening during plastic deformation.

2. Experimental details

2.1 Material preparation

TWIP steel with the composition shown in **Table 1** was melted in an Ar-filled vacuum furnace and then hot rolled to obtain 10 mm thick sheets. The sheets were cold rolled several passes into sheets with a thickness of 2 mm containing fine grains with an average grain size of about 8.49 μm. 2 mm thick sheets were rolled in a two-roll cold mill with rolling stresses $\leqslant$ 1500 KN on one side to produce sheets by adjusting the different press-down displacements and combining them with the stress relief annealing. Specifically, the sheets with a thickness of 2 mm were cold rolled to ~1.2 mm and then annealed at 700 °C for 10 min (the first cycle). Then, the annealed sheets were cold rolled to ~0.8 mm and annealed at 700 °C for 10 min (the second cycle). The sheets processed in the second cycle were finally cold rolled to ~0.6 mm.

Table 1. Chemical compositions of the experimental TWIP steel (mass fraction, %)

C	Mn	Si	Al	S	P	Ti	Fe
0.59	15.68	0.074	1.19	0.006	0.008	≤0.01	Bal.

Some grains in the final sheets obtained were elongated along the rolling direction (RD). These grains with high internal stresses were not favourable for obtaining a clear microstructure

in the in-situ tensile experiments. Therefore, the annealing process was carried out in a staged heating mode from room temperature to 600 °C at a rate of 10 °C/min, and then to 700 °C at a rate of 3 °C/min, holding for 10 min and then cooling. Finally, combining the rolling and annealing, referring to this work [27], the schematic illustration of thermo-mechanical process route for experimental steels is summarized in **Fig. 1**. TWIP steels with fine and ultrafine grains were prepared, which provided important raw material support for subsequent experiments.

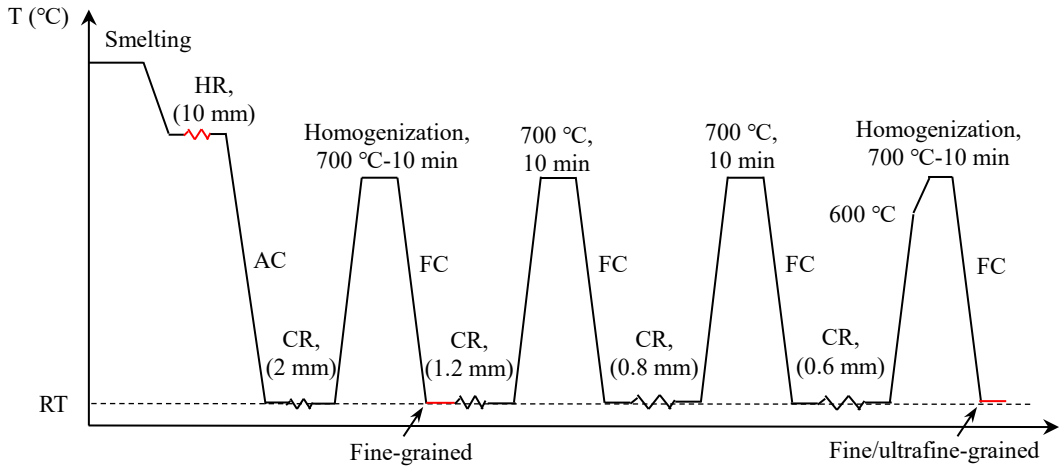

Fig. 1. The Schematic illustration of thermo-mechanical process route of fine-grained and fine-/ultrafine-grained TWIP steels. T: temperature, RT: room temperature, HR: hot rolling, CR: cold rolling, AC: air cooling, FC: furnace cooling.

2.2 In-situ EBSD characterisation of tensile tests

The fine-/ultrafine-grained TWIP steel sheets were processed by molybdenum wire-cut electrical discharge machining method [39] to obtain rectangular dog-bone-shaped tensile specimens, as shown in **Fig. 2**(a). The specimens were then ground until the surface was flat and smooth without obvious defects. Then electrochemical polishing was carried out with 10% perchloric acid-ethanol ($HClO_4$-C_2H_5OH) electrolyte solution [40] in an ice-water bath at a voltage of 20 V for 40-60 s to remove the damaged surface. As shown in **Fig. 2**(b), the initial microstructure in the gauge region is composed of typical equiaxed austenite grains with FCC lattice type. The tension axis (TA) is parallel to the RD. The grain size distribution is presented in **Fig. 2**(c).

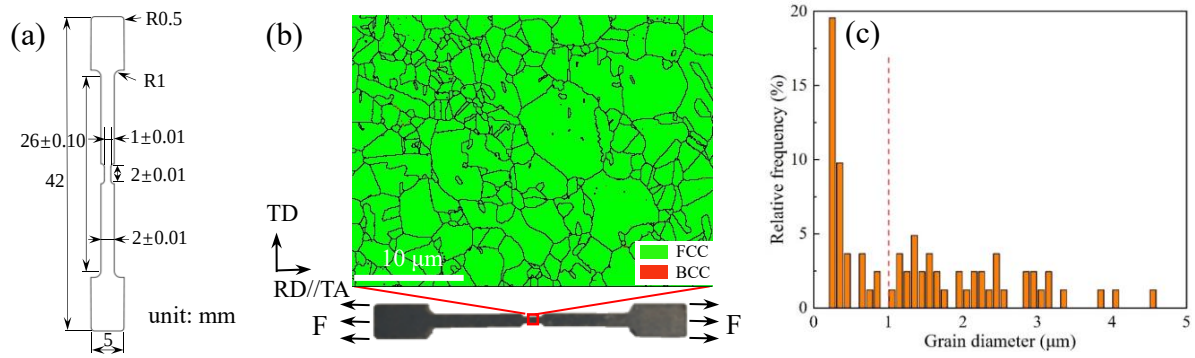

Fig. 2. In-situ EBSD tensile (a) specimen and its dimensions, (b) EBSD phase distribution map of initial microstructure and (c) the grain size distribution of fine and ultrafine grains.

The self-developed bidirectional trapezoidal screw in-situ tensile testing device and control system were employed for micromechanical tests. The tensile rate was set to 1 μm/s ($5\times10^{-4}s^{-1}$) along the RD and the values of displacement and load were recorded by displacement and force sensors. Meanwhile, a field emission electron microscopy (FEI Quanta 650 FEG SEM) equipped with an EBSD probe (EDAX-TSL) was utilized to capture the microstructural information during the in-situ loading. The step size was set to 0.05 μm. Simultaneously, local EBSD imaging was performed in the observation area to explore the microstructural features at different strains to analyse the potential origin of the excellent mechanical properties.

2.3 TEM characterisation of interrupted strain tests

For the interrupted strain tests, the dog-bone-shaped specimens with a gauge section of $10\times3\times0.6$ mm^3 were prepared by molybdenum wire-cut electrical discharge machining. Then, the specimen was clamped in a universal testing machine (WDW-200). The loading rate was 0.6 mm/min, i.e., the strain rate of 10^{-3} s^{-1}. The tensile axis (TA) was parallel to the RD. Different specimens were loaded to strains of 0.1, 0.2, 0.3, 0.4 and fractured, respectively.

After unloading the tensile specimens at predetermined strains, their gauge sections were cut into the thickness of ~0.5 mm flat specimens using electrical discharge machining and then ground to <100 μm using 800-grit SiC sandpaper. Discs of 3 mm diameter were then prepared

by stamping and ground to a <75 μm foil using 1200-grit SiC sandpaper. Finally, the discs were further thinned to perforation by double-jet electrochemical polishing at 20 V and -30 °C using an electrolyte solution consisting of 90 vol.% methanol and 10 vol.% perchloric acid. TEM characterisation was carried out using an FEI Tecnai F30 instrument operating at 200 kV.

3. Results

3.1 Mechanical properties

The true stress-strain curves of TWIP steels are obtained based on the tensile tests, as shown in **Fig. 3**(a), where the solid red circle markers are stop points for EBSD observation in the in-situ tensile test. It can be intuitively seen that the YS and ultimate tensile strength (UTS) of the fine-/ultrafine-grained TWIP steel are elevated while the uniform elongation (UE) is slightly decreased compared to the fine-grained TWIP steel. The increase in YS adapts to the empirical Hall-Petch equation, given by fitting: YS=143.1+184.1/$\sqrt{d}$. The fine-/ultrafine-grained TWIP steel presents excellent mechanical properties, which is directly related to the higher strain hardening rates illustrated in **Fig. 3**(b).

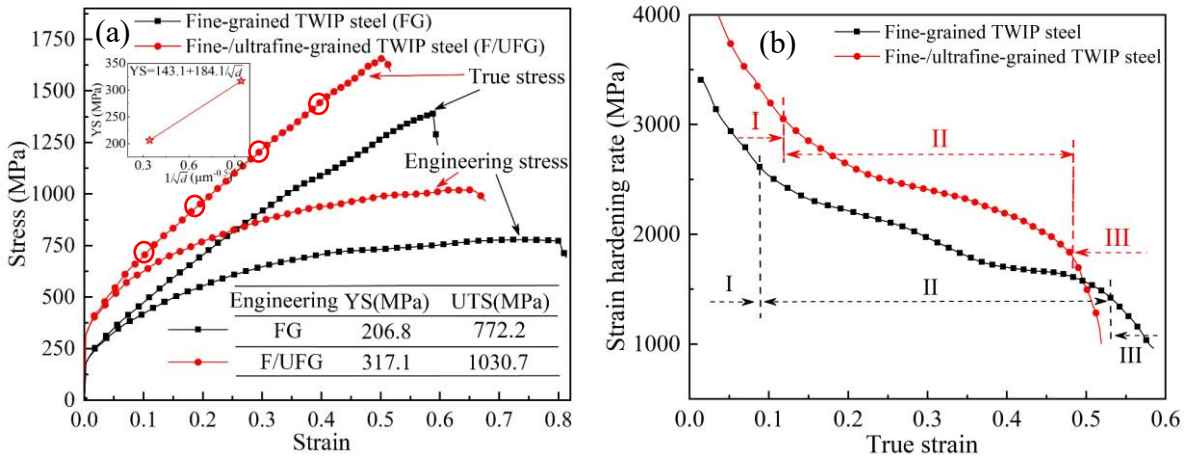

Fig. 3. Mechanical properties of fine-grained and fine-/ultrafine-grained TWIP steels: (a) stress-strain curves and (b) strain hardening rate curves. The solid red circle markers are stop points for EBSD observation in the in-situ tensile test.

Clearly, the strain hardening process can be divided into three stages according to the changes in the slope [33], with a rapid decrease from higher values in stage I to a smooth stage

II, which is the result of the coupling effect of complex deformation mechanisms [15, 41]. The fluctuations in stage II for fine-grained TWIP steel are attributed to the fact that mechanical twins become more active [33]. Then after a slow decline, the strain rate reaches ~0.5, entering stage III, which is often accompanied by damage accumulation and plastic instability before fracture [42]. It is noteworthy that the fine-/ultrafine-grained specimen maintains higher strain hardening rates in both stages I and II, the underlying reasons here need to be further explored.

The UTS and UE were extracted based on experimental data. The product of strength and elongation (PSE) of engineering was calculated. In particular, the engineering UTS of the fine-/ultrafine-grained TWIP steel is higher than 1000 MPa. The UTS-UE of some typical steels including fine-grained and ultrafine-grained steels in references [5, 11, 14, 15, 29, 33, 43-47] is compared and the results are shown in **Fig. 4**. Clearly, the TWIP steels in this work have excellent mechanical properties. Their PSEs all exceed 60 GPa·%. Particularly, the fine-/ultrafine-grained TWIP steel has a higher PSE, ~71 GPa·%. Undoubtedly, such results can indicate an improvement in the strength-plasticity trade-off difficulty [48]. Thus, it is crucial to elucidate the underlying deformation mechanisms to exploit their potential for industrial applications.

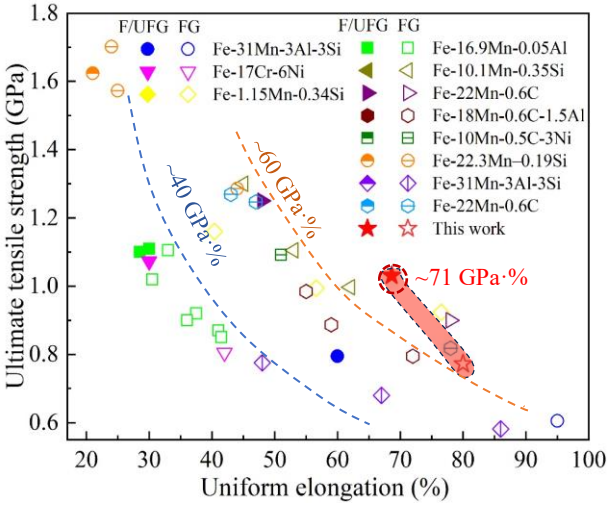

Fig. 4. Comparison of the ultimate tensile strength-uniform elongation of this work with that of references [5, 11, 14, 15, 29, 33, 43-47]. F/UFG: fine/ultrafine-grained, FG: fine-grained.

3.2 Microstructural evolution

To further investigate the microstructural evolution of the fine-/ultrafine-grained TWIP steels with excellent properties during plasticity deformation, the in-situ EBSD method provides a reliable solution strategy. **Fig. 5** shows the microstructural evolution characterised by inverse pole figures (IPFs) during the in-situ tensile test at different strains of 0.1, 0.2, 0.3 and 0.4. The microstructure of the undeformed specimen is presented in **Fig. 5**(a). To further explore the different deformation mechanisms of grains with different orientations, sizes and positions, four different typical sets in the monitoring area are marked as Set 1, Set 2, Set 3 and Set 4 with several grains respectively, where Set 4 consists totally of ultrafine grains. It is worth noting that at ε=0.4, due to the limitation of the scanning range, only a portion of the full region is selected to detect, where Set 2 and Set 3 are not included.

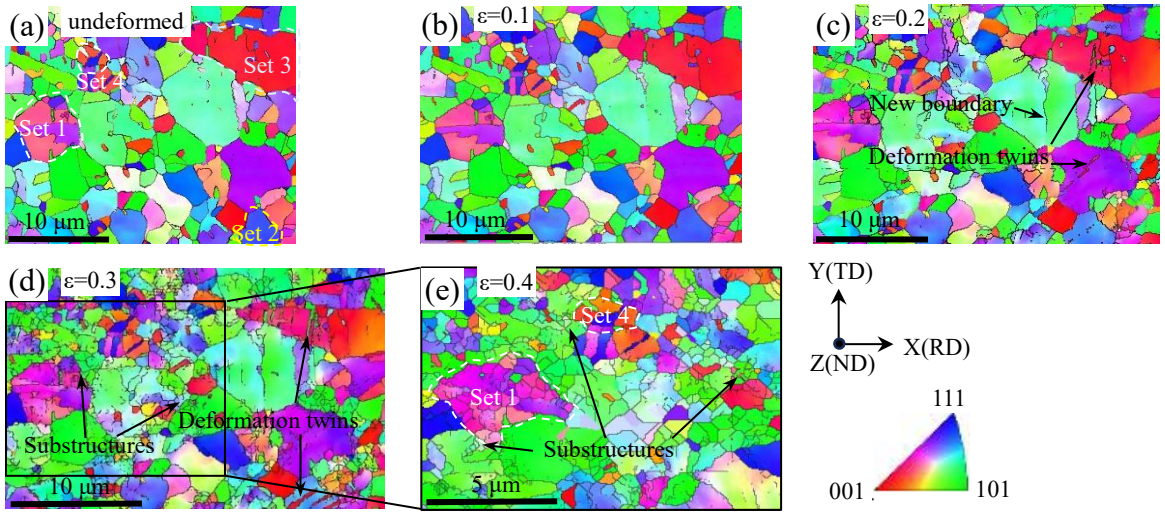

Fig. 5. IPFs of microstructures of the fine-/ultrafine-grained specimen at different strains: (a) undeformed, (b) ε=0.1, (c) ε=0.2, (d) ε=0.3, (e) ε=0.4.

With the increase of strain, all grains are significantly elongated, and deformation twins are present in some grains at ε=0.2 in **Fig. 5**(c), which is consistent with the findings [45]. In addition, new boundaries appear in some grains elongated along the TA direction. These deformation twins and boundaries are further extended and grown at ε=0.3 in **Fig. 5**(d). Meanwhile, many substructures [45, 49] are generated near the GBs, which may be the result

of dislocation pile-up and stacking fault development. Next, when the strain increases to 0.4, it can be found that there are large differences in the orientation of different positions in some grains, which are gradually broken into several subgrains in Set 1. The formation of subgrains can further coordinate deformation and delay the fracture [38, 50], while the reduction in grain size increases the strength and hardening rate.

To elucidate the relationship between plastic deformation and grain orientation, the (100) polar figures (PFs) of different strains are depicted in **Fig. 6**. Statistically, there is no obvious change in the orientation distribution in **Fig. 6**(a)~(d), and this also confirms that the subgrains generated by the dislocation accumulation have a limited effect on the grain orientation distribution of all grains. A small number of deformation twins have a negligible effect on the overall distribution results of grain orientation. The significant distribution difference in **Fig. 6**(e) is intimately related to the selected local region.

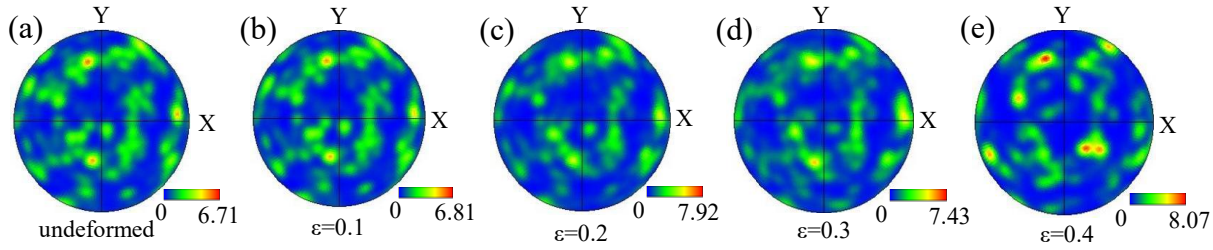

Fig. 6. (100) PFs of microstructures of the fine-/ultrafine-grained specimen at different strains: (a) undeformed, (b) ε=0.1, (c) ε=0.2, (d) ε=0.3, (e) ε=0.4.

Combined with the microstructural evolution based on EBSD-IPFs and EBSD-PFs, the dislocation accumulation needs to be explicitly elaborated to explore the distribution of plastic deformation between and in grains. **Fig. 7** illustrates the kernel average misorientation (KAM) distribution of the fine-/ultrafine-grained specimen at different strains. The KAM values of undeformed specimen near GBs are low and negligible. Different KAM values are represented by different colours in the figure, blue for the lowest value (0°) and red for the highest (5°). It can be seen that the red area maintains increasing with strain, which implies that the KAM is increasing moderately. It is also noted that the KAM values near the GBs are generally higher.

Due to the close relationship between KAM and GNDs, GND density can be calculated based on the KAM with the following equation [51, 52]:

$$\rho_{GND} = \frac{2\theta_{KAM}}{\mu b} \quad (1)$$

where ρ_{GND} is the GND density; θ_{KAM} represents the local misorientation in the KAM maps [51]; b=0.25 nm is the magnitude of the Burgers vector [22]; $\mu=kl$ is the kernel size [53], where k is the defined nearest neighbour and l is the scan step [54]. Thus, the KAM maps can directly present the distribution of GND density. Consequently, the red colour area means that the GND density is higher, where the dislocation pile-up is more significant.

Furthermore, severe lattice distortions are produced near the GBs due to the large number of dislocations pile-up in **Fig. 7**(d) and (e), resulting in an unclear display of the KAM values here. Combined with the trend of dislocation distribution near GBs in **Fig. 7**(a)~(d), these unidentifiable regions due to lattice distortion should have higher KAM values. However, they are regarded as regions with lower KAM values, which introduces some errors in the statistics. These unidentifiable regions are exactly the locations of subgrain distribution generated by the higher GND density in **Fig. 5**(d) and (e).

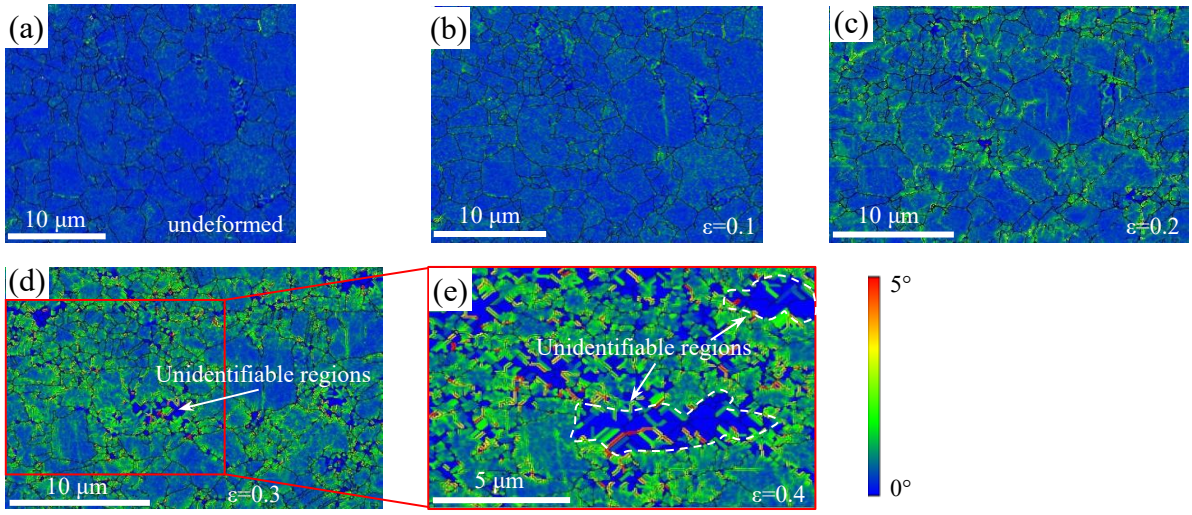

Fig. 7. KAM maps of microstructures of the fine-/ultrafine-grained specimen at different strains: (a) undeformed, (b) ε=0.1, (c) ε=0.2, (d) ε=0.3, (e) ε=0.4.

4. Discussion and analysis

4.1 Distribution of misorientation angle

Since GBs become the main dislocation sources and sinks when the grains are smaller than the critical size [33, 37], their distribution and type frequency directly affect the activation of plastic deformation mechanisms. The deformation twins generated at large strains also introduce new boundaries in **Fig. 5**, which dynamically reduces the average grain size. Meanwhile, based on the EBSD-IPFs, the subgrain generation due to dislocation accumulation can further induce the generation of new boundaries [55, 56]. Although these boundaries are almost low angle grain boundaries (LAGBs), they can affect the distribution of the misorientation angle and also contribute to the reduction in grain size. All these factors can enhance the strain hardening and delay the appearance of microcracks.

Fig. 8 illustrates the distribution of misorientation angles calculated based on the EBSD data. Here, the nearly perfect misorientation angle of ~60° indicates the typical $\sum 3\{111\}$ coherent twin boundaries. It can be noticed that the LAGBs increase while the twin boundary fraction gradually decreases with increasing strain, which seems to contradict the previous conclusions [40, 57]. To elucidate the potential reasons leading to this phenomenon, the evolution of the deformation twin boundary fraction is presented in **Fig. 8**(b) based on the previous self-developed code [40] characterizing the ratio of pixel size for the corresponding colours of the GBs and twin boundaries in the overlapping EBSD maps. It is worth noting that the results here exclude the annealing twin boundaries in the undeformed state, so they are able to directly elucidate the evolution of deformation twins. However, the appearance of deformation twin boundaries is not detected before ε=0.2, implying that dislocation slip dominates plasticity in this stage. With increasing strain, the deformation twin boundary fraction decreased from 2.0% at ε=0.2 to 1.2% at ε=0.4. However, the deformation twin boundary fraction increased from 2.1% at ε=0.2 to 16.9% at fracture in the TWIP steel with an

average grain size d=10.5 μm [40]. On the one hand, as the plastic deformation continues, the GND density near the GBs increases, resulting in the lattice orientation mismatch here, which further promotes the formation of subgrains [55] and new boundaries, thus greatly enhancing the LAGBs fraction [11]. On the other hand, the rapid accumulation of dislocations induced by plastic deformation in the fine-/ultrafine-grained TWIP steels increases the back stress on the dislocation in the slip plane [58]. The higher back stress narrows the width of stacking faults, facilitates the cross slip of dislocations, and reduces the interactions between partial dislocations required for mechanical twinning, which inhibits twinning [33]. Indeed, this conclusion is confirmed by the fact that lamellar deformation twins with significant thicknesses are found in only a few fine grains in **Fig. 5**. This is another key factor for the reduction of the deformation twin boundary fraction.

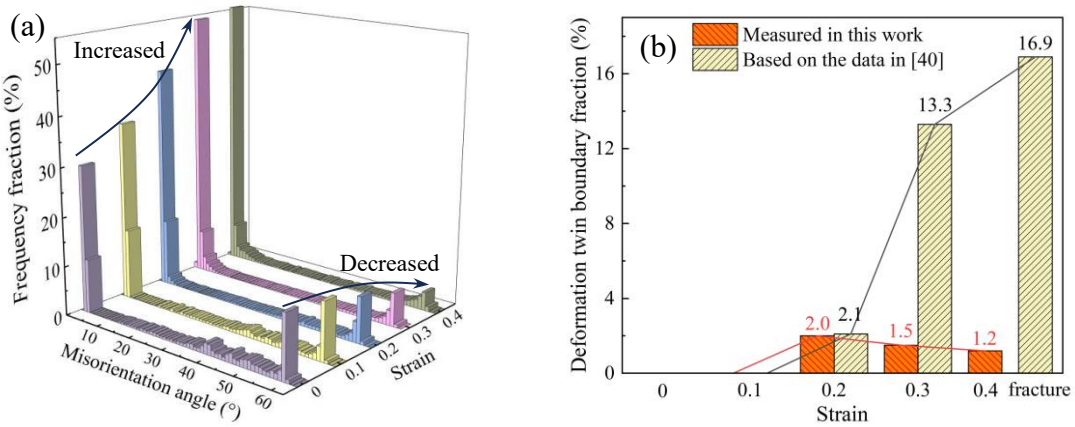

Fig. 8. (a) The distribution of misorientation angle in the test. (b) Comparison of deformation twin boundary fractions between the fine-/ultrafine-grained (this work) and coarse-grained [40] TWIP steels at different strains.

4.2 Evolution of typical features

It is well-known that the SPD can effectively reduce grain size without changing the alloy composition [43, 45, 59-61]. To explore the deformation behaviour of grain interior, the IPFs of the Set 1~Set 4 selected at different strains in **Fig. 5** are exhibited in **Fig. 9**, where Set 1~Set 3 are mainly composed of fine grains and Set 4 is filled with ultrafine grains. It is clear that the

micromechanical behaviour of the grain interior is affected by the grain orientation. Specifically, no mechanical twins are observed in Set 1 and Set 4 during all deformation stages, whereas obvious deformation twins are observed in Set 2 and Set 3 with different orientations. As a result, the average grain sizes of Set 2 and Set 3 are dynamically reduced due to the partitioning of the deformation twins. Also, the average grain sizes of Set 1 and Set 4, where plastic deformation is dominated by slip, are also reduced due to subgrains generation in **Fig. 9**(e).

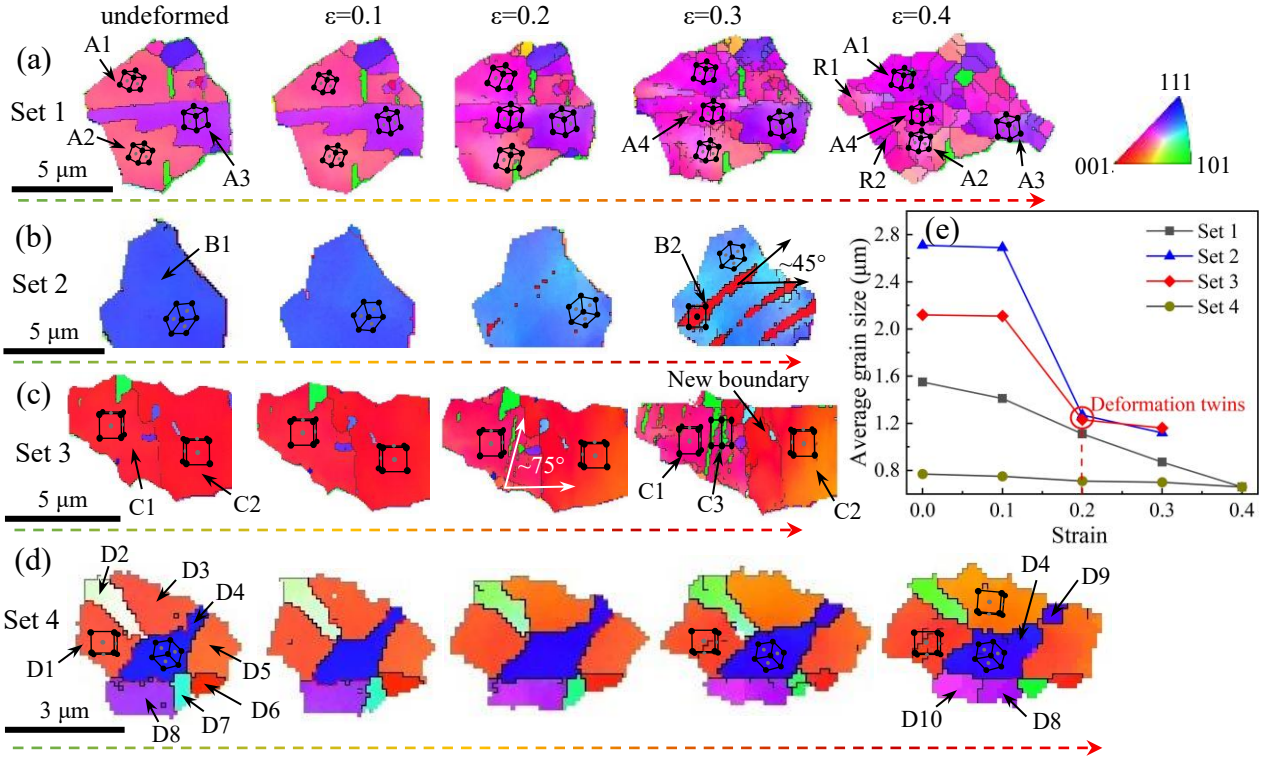

Fig. 9. IPFs of different grain sets in the in-situ EBSD tensile test under uniaxial tensile: (a) Set 1, (b) Set 2, (c) Set 3 and (d) Set 4 marked in **Fig. 5**. (e) Variation of the average grain size with strain for Set 1-Set 4.

Carefully, it should be noticed that the several grains marked in **Fig. 9**(a), in Set 1 at ε=0.3, grain A3 is broken into two grains along the loading direction. Obviously, the newly generated grain A4 has a different orientation from the grain A3. As the strain increases to 0.4, many subgrains are produced to coordinate the larger deformation. In contrast, in Set 2 of **Fig. 9**(b), the new twins further refine the grain B1, and the angle between the twin B2 and the loading direction is ~45°, which is consistent with the direction of maximum shear stress. This looks

different from the angle between the twin C3 and the loading direction is ~75° in **Fig. 9**(c), where the matrix grain C1 is close to the grain orientation of the neighbouring grain C2. Unexpectedly, the twin does not appear in grain C2, but a new boundary is generated, suggesting that the nucleation of twins may be related to local stresses [14, 24] in addition to grain orientation. For Set 4, when the strain increases to 0.4, all grains are elongated while local grains clearly rotated, e.g. grains D1 and D2. Also, some grains are broken from one grain into two grains, e.g. grains D9 and D10 are separated from grain D4 and D8, respectively. In this respect, it is similar to the deformation behaviour of Set 1.

To further elucidate the dislocation activity of different grains, the KAM distributions of Set 1~Set 4 are presented in **Fig. 10**. The different grain sets indicate that the KAM values increase with strain and their distribution is very heterogeneous, mainly concentrated near GB and some subgrains. As shown in **Fig. 10**(a), the KAM values are larger at the grain edges, implying a higher GND density here when ε=0.4. Therefore, the local lattice of these grains may actively rotate here due to GNDs pile-up [50], eventually leading to the formation of subgrains R1 and R2. However, the KAM values near the twin boundaries in **Fig. 10**(b) are not high, whereas they are higher in **Fig. 10** (c). Meanwhile, the GNDs gathered near the twins and grain boundaries in **Fig. 10**(b), suggests that the growth of deformation twins can relieve the local stresses to further promote dislocation multiplication [28, 40]. The high KAM near the newly generated boundary in **Fig. 10**(c) suggests that the aggregation of GNDs allows the grain C2 to rotate locally, thus contributing to the generation of new boundaries [50].

For Set 4 composed of ultrafine grains in **Fig. 10**(d), GNDs are mainly concentrated near the GBs due to the limitation of grain size. The difference is the newly generated grain D10 has a higher GND density while grain D9 does not. Grain D10 separated from grain D8 reveals that high GND density can induce the generation of subgrains even in the ultrafine grains. The grains D9 may be partially lattice rotation due to tensile deformation resulting in separation of the

grains D4. The statistical results of the KAM distributions of all four grain sets are shown in **Fig. 10**(e), where they are more dispersed and less frequency different as the strain increases. Meanwhile, the peaks of their distribution move to a higher value, indicating an increase in the average KAM values of the grain sets.

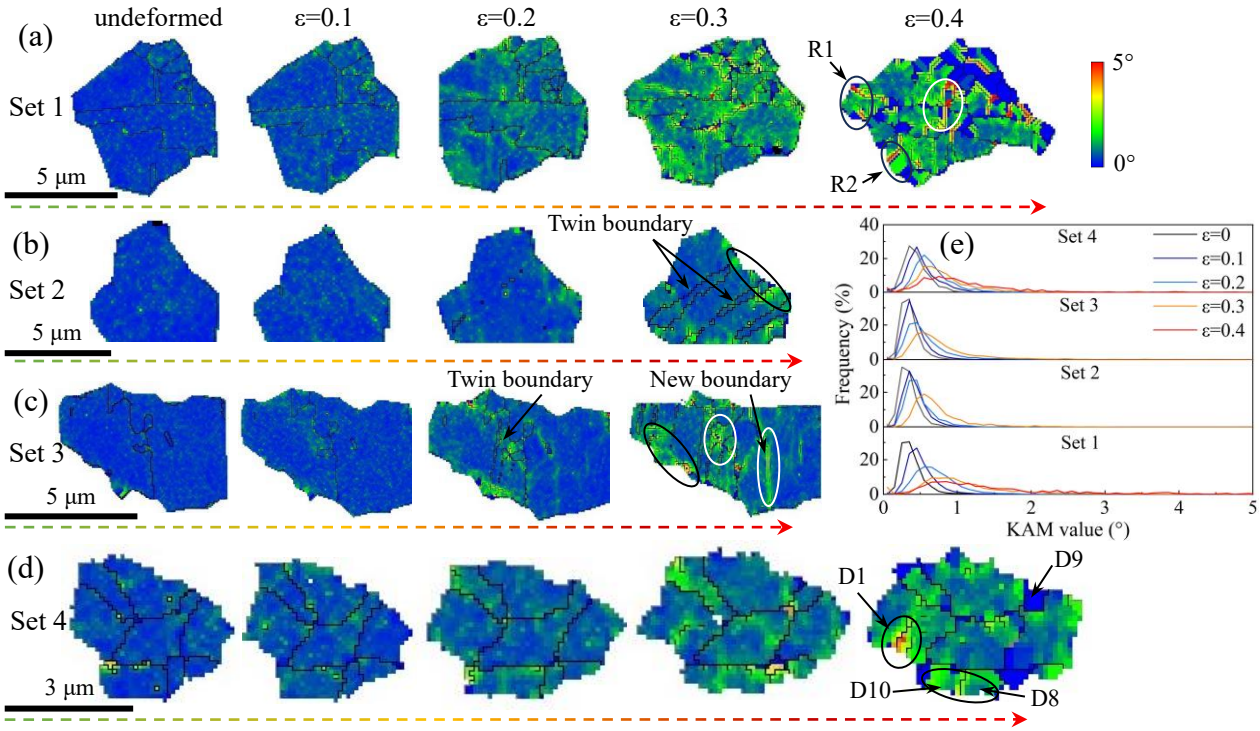

Fig. 10. KAM distributions of different sets in the in-situ EBSD tensile test: (a) Set 1, (b) Set 2, (c) Set 3 and (d) Set 4, where circles indicate higher KAM values. (e) Statistics of KAM distribution of Set 1~Set 4.

4.3 Evolution of GND density

Based on the average KAM values of all grains in **Fig. 7** and Set 1~Set 4 in **Fig. 10**, the results are shown in **Fig. 11**(a). The difference in the KAM maps of Set 1~Set 4 reveals that the average KAM values are regulated by the microstructures induced by different deformation mechanisms [52, 57]. Obviously, the average KAM values of Set 2 and Set 3 with twinning-mediated plasticity are lower than those of Set 1 and Set 4 with slip-dominated plasticity, and the average KAM value of Set 2 is the lowest while that of Set 1 is the highest, which is attributed to the dislocation pile-up promoting the formation of subgrains in Set 1, further

hindering dislocation motion [55] and resulting in an increase in KAM values. In contrast, Set 2, which relies on twinning to relieve local stress concentration, presents low KAM values in the twinned region. Indeed, both subgrains generated by dislocation slip and twin boundaries introduced by twinning reduced the local grain size, thus exacerbating dislocation pile-up near boundaries to enhance strain hardening.

It is widely expected that the poor plasticity of nano/ultrafine-grained metals is usually due to the limited strain hardening capability in the ultrafine and complicated deformation microstructure with highly stored dislocations where it is difficult to introduce more dislocations [62]. Therefore, it is crucial to explore the evolution of dislocation density to further improve the material strength and ductility. Eq. (1) reveals the relationship between KAM and GND density, which is an important basis for microstructural deformation inhomogeneity. The GND density can be calculated based on Eq. (1) and the results are shown in **Fig. 11**(b). Meanwhile, the GND density can be estimated using the typical Ashby′s model [63]. Considering the effect of deformation twins on the MFP of dislocations, Ashby′s model can be modified using the following equation [22]:

$$\rho_{\mathrm{GND}} \cong \frac{\varepsilon}{4b}\left(\frac{1}{d}+\frac{F}{2e(1-F)}\right) \tag{2}$$

where ε is the macroscopic plastic strain, b is the magnitude of the Burgers vector and d denotes the average grain size. F and e are the volume fraction and the mean thickness of the deformation twins [22, 64].

In fact, twin boundaries and GBs have been considered when calculating grain size based on EBSD-IPFs. Therefore, ρ_{GND} is estimated based on the average grain size in real time. The estimated ρ_{GND} is compared with the measured results in **Fig. 11**(b). Due to the smaller average grain size of Set 4 in **Fig. 9**(d), the estimated ρ_{GND} is higher compared to the others. However, the average grain sizes of Set 1~Set 3 are larger while the activation of different deformation

mechanisms in the grains results in larger differences in GND density, so the error between their estimated and measured ρ_{GND} of all grains is larger. Carefully, it can be noticed that the measured ρ_{GND} is slightly higher than the estimated ones, which may be attributed to the microstructure inhomogeneity promoting the GND density in the test [13].

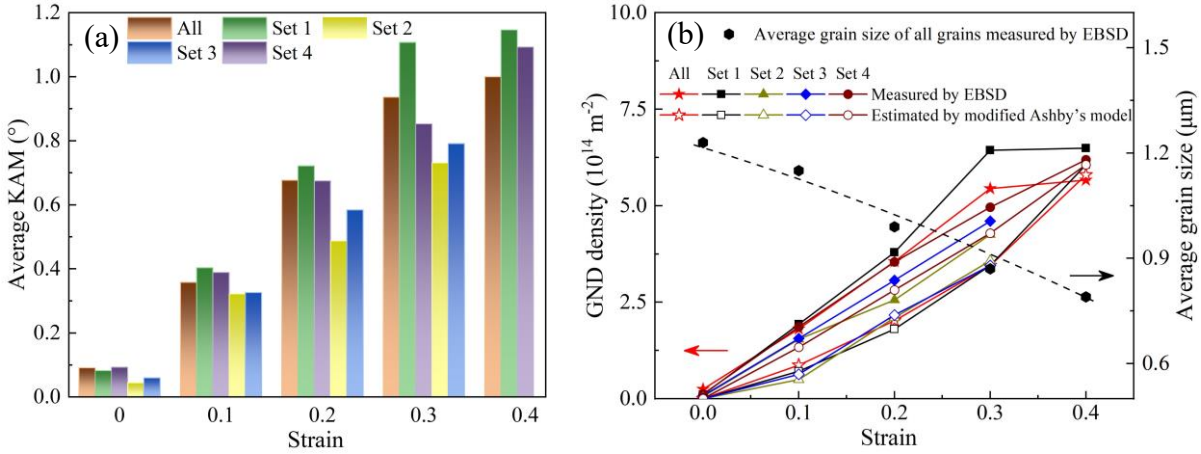

Fig. 11. (a) The average KAM and (b) GND density of all grains and Set 1~Set 4. The average grain size of all grains and the evaluated GND density based on the modified Ashby's model are included in (b).

4.4 Evolution of dislocation and stacking fault

The average KAM of Set 1 is slightly lower than that of Set 4 when undeformed, whereas the average KAM of Set 1 is slightly higher than that of Set 4 at ε=0.1 and remains until fracture in **Fig. 11**, which suggests that the activated deformation mechanisms may be different for fine and ultrafine grains at initial deformation. Also, there is no significant lamellar twin in ultrafine grains during the overall deformation stages. To further reveal the inherent reasons for these phenomena, more critical observations based on TEM are needed [65]. Hence, specimens with different pre-strains were obtained by utilizing interrupted strain tests and their microstructures were characterised by TEM to elucidate the microstructural evolution during strain hardening.

Annealing twins can be seen in the bright field (BF)-TEM image of the undeformed specimen in **Fig. 12**(a) and the selected area electron diffraction (SAED) patterns in **Fig. 12**(b). Meanwhile, there are no obvious defects in the ultrafine grain in **Fig. 12**(c) and the regular

arrangement of atoms on both sides of the GB can be clearly seen by high resolution transmission electron microscopy (HRTEM) in **Fig. 12**(d), and no obvious defects or second phase particles are observed here. As the strain increases to 0.1, a large number of dislocations are activated and dislocation walls are formed in the fine grain with a grain size of 2.1 μm in **Fig. 12**(e). Due to the activation of different slip systems and their interaction, an angle of ~60° is presented. In **Fig. 12**(f), dislocations are activated in the ultrafine grain with a grain size of 0.85 μm but no obvious dislocation substructure appears. The reduction of grain size can elevate the CRSS for slip, slip thus is preferentially activated in the fine grains at the same local stress. The HRTEM image in **Fig. 12**(g) indicates that more stacking faults are formed near the GBs due to the activation of Shockley partial dislocation, which is confirmed by the results of SAED pattern in **Fig. 12**(h).

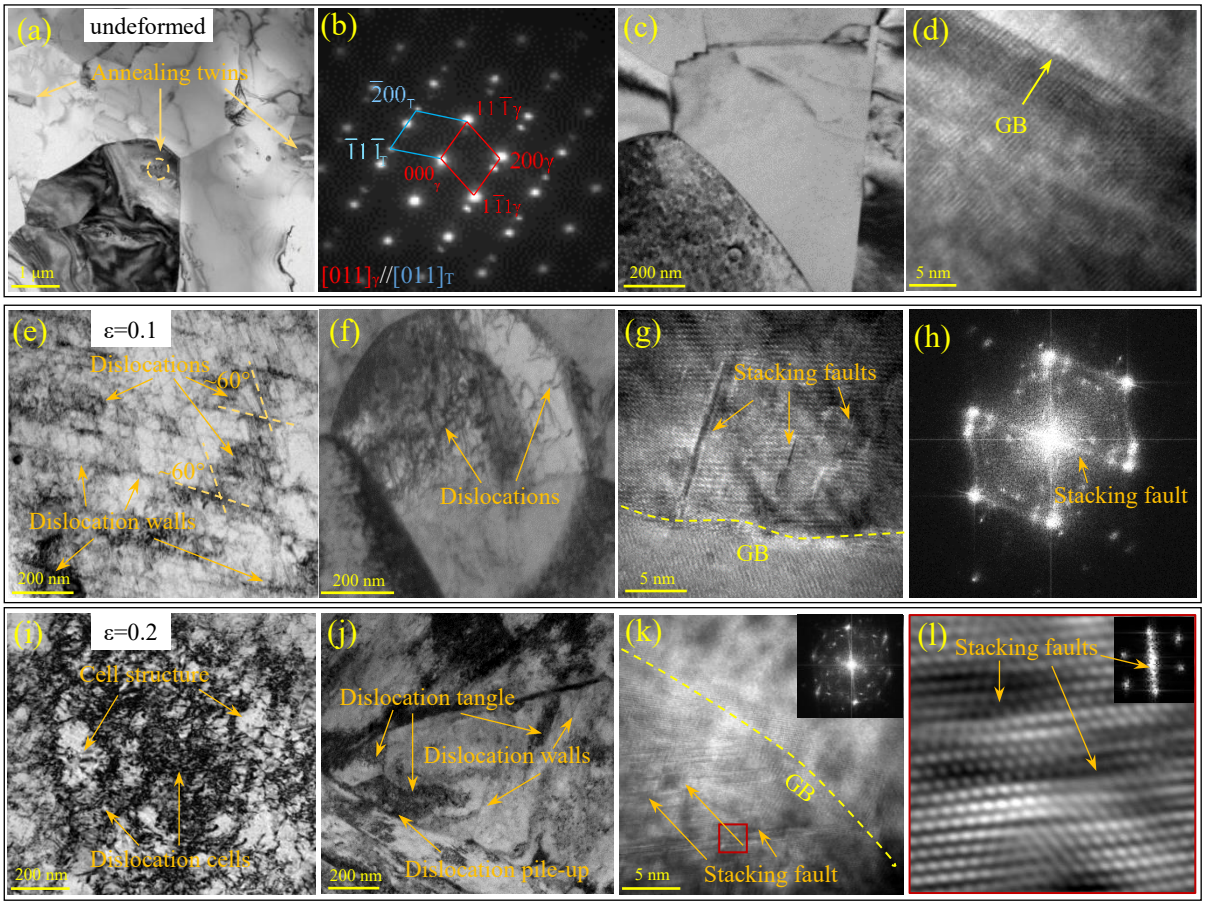

Fig. 12. Representative microstructures and defects in fine-/ultrafine-grained specimens. (a) Annealing twins and (b) SAED patterns, (c) ultrafine grain with a grain size of 0.69 μm and

(d) HRTEM image near GBs of the undeformed specimen. Dislocation substructures in (e) the fine grain with a grain size of 2.1 μm and (f) the ultrafine grain with a grain size of 0.85 μm, (g) stacking faults near GBs and (h) corresponding SAED pattern of the specimen deformed to ε=0.1. Dislocation substructures in (i) fine and (j) ultrafine grains, (k) stacking faults near GBs of the specimen deformed to ε=0.2, (l) HRTEM image of the local area in (k).

When the strain increases to 0.2, more dislocations are activated and the interactions between dislocations successively form dislocation cells and cell structures as demonstrated in **Fig. 12**(i). Due to the grain size limitation, several dislocation walls and dislocation tangles appear in ultrafine grains in **Fig. 12**(j). Meanwhile, dislocations pile-up near the GBs due to the blocking effect of GBs, which further enhances strain hardening. More stacking faults are formed near the GBs that act as the sources of dislocation emission in **Fig. 12**(l). When ε=0.3 in **Fig. 13**(a), many deformation twins appear in fine grains. It is accepted that stacking faults can contribute to the generation of twins. Shockley partial dislocations were emitted and formed the stacking fault near GBs [37, 65], and the nucleation of deformation twins was further facilitated by more partial dislocations moving near the stacking fault [66]. It is also commonly believed that deformation twins in alloys are nucleated by the dissociation of pre-existing dislocations into partial dislocations, which can form multi-layered stacking faults. All require the glide of partial dislocations with Burgers vector of a/6 [112] on success $\{111\}$ planes [28]. Moreover, the twin boundaries are barriers to dislocation motion, which promotes dislocation-twin interactions and the formation of dislocation cells and dislocation walls between the twin lamellas, as shown in **Fig. 13**(b). Meanwhile, in **Fig. 13**(c), many stacking faults (L3) are found in the matrix grains according to the HRTEM image, and some of these stacking faults develop into twins (L2) due to the aggregation of partial dislocations, which can be named as nano-twins because they are very thin [67, 68] and the thickness is only ~5 nm. In addition, the SAED patterns in the local area (L4) reveal that the interaction of the stacking faults can form the

Lomer-Cottrell locks (LCs) [69, 70], which act as a strong obstacle for further dislocation motion on two (111)-type slip planes and thus enhancing strain hardening.

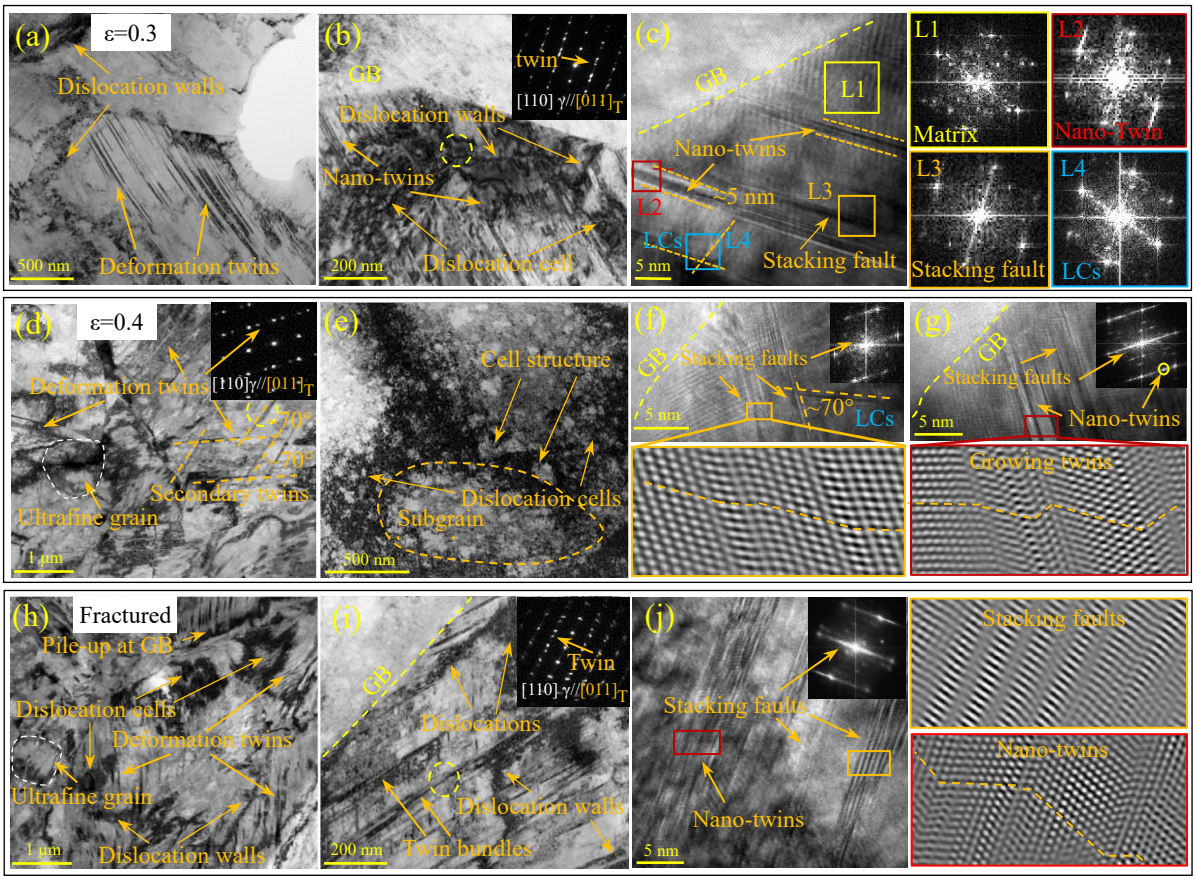

Fig. 13. Representative microstructures and defects in fine-/ultrafine-grained specimens deformed from ε=0.3 to fracture. (a) Layered deformation twins, (b) dislocation substructures generated by the interaction of dislocations, deformation twins and GBs, (c) Matrix (L1), nano-twins (L2) and stacking faults (L3) formed by the accumulation of Shockley partial dislocations near GB and LCs (L4) generated by stacking faults interactions when ε=0.3. (d) Interaction of primary and secondary twins, (e) dislocation substructures and subgrains, (f) developing stacking faults and (g) growing nano-twins and their HRTEM images at ε=0.4. (h) BF-TEM image of microstructures and (i) intertwining of twin bundles and dislocation substructures, (j) HRTEM images of stacking faults and nano-twins of fractured specimens.

Twin nucleation near GBs may become more frequent with increasing strain. Meanwhile, the different degree of the motion of twinning partial dislocations suggests a different degree

of growth kinetics of deformation twins depending upon the local stresses [65]. In this work, the nucleation and development of LCs and nano-twins suggest that GBs can continuously emit several Shockley partial dislocations [41]. Generally, Shockley partial dislocations move in an inclined twin confined between a precipitate and a stacking fault, thereby leading to the growth of the deformation twin [65]. Meanwhile, the SFE (γ_{SFE}=27.8 mJ/m^2) is calculated from the thermodynamic model [17], which permits a dislocation to be dissociated into two Shockley partial dislocations, leading and trailing, with a stacking fault between them [2]. This further elucidates the underlying reason for the appearance of stacking faults and nano-twins near the GB in **Fig. 13**(c). The strain increases to 0.4, different twin systems are activated to interact with primary twins in fine grains in **Fig. 13**(d), and the angle between the primary and secondary twins is approximately 70°. In some grains, subgrain formation is induced by the development of dislocation cells and cell structures [4, 55] (**Fig. 13**(e)). For ultrafine grains, the stacking faults are activated to form LCs with ~70° angle in **Fig. 13**(f) and previous stacking faults grow into nano-twins, resulting in an increased number of nano-twins and orderly distribution in the grains as shown in **Fig. 13**(g).

As the grain size decreases to ultrafine grain scale, the GB-mediated plastic deformation mechanism becomes active [2], which is confirmed in the BF-TEM images of the microstructure at the fracture. In **Fig. 13**(h), it can be seen that the deformation twins are densely distributed and intertwined in fine grains, and the GBs become fuzzy due to high local stresses caused by the dislocation pile-up. The interactions between dislocation walls, dislocation cells and deformation twins are more prominent. **Fig. 13**(h) demonstrates the formation of twin bundles, where the lamella-by-lamella twins are developed by the embedded stacking faults. The dislocation substructures are more pronounced, which facilitates subgrains generation and grain rotation, resulting in further grain refinement. This is consistent with the finding that the frequency of LAGBs found in the in-situ EBSD test increases at higher strains in **Fig. 8**.

Meanwhile, the HRTEM images and SAED patterns of ultrafine grains in **Fig. 13**(j) reveal the development of stacking faults and growth of nano-twins, suggesting that stacking faults and nano-twins play an important strengthening and toughening role during plastic deformation.

Interrupted strain experiments and TEM characterisation reveal that stacking faults and deformation twins are intimately related to GBs. Dislocations are preferentially activated in fine grains, and ultrafine grains require higher local stresses to activate slip due to the elevated CRSS for slip. With increasing strain, stacking faults and nano-twins in ultrafine grains mediate plastic deformation while dislocation and their substructures and laminar deformation twins in fine grains dominate plastic deformation. It is also elaborated that deformation twins and stacking faults reduce the MFP of dislocations, which exacerbates the subsequent dislocation-twin and twin-twin interactions, resulting in intertwined dislocation substructures interacting with stacking fault substructures, thus enhancing strain hardening. Notably, LCs and nano-twins are found in this investigation to enhance strain hardening as well. Coherent twin boundaries serve as an important location for deformation localisation in the grain, while misorientation and high strain gradients can occur nearby [71], which is likely to be a precursor for crack initiation.

5. Deformation mechanisms of the fine-/ultrafine-grained TWIP steels

The deformation mode may be influenced by grain orientation and local stress variations at the grain scale [24] in addition to grain size [2]. Under low strain levels, the activation of slip and twinning is regulated by the respective critical shear stress. Therefore, the fact that the fine-/ultrafine-grained TWIP steel exhibits a higher strain hardening rate in **Fig. 3** may be intimately related to the grain size (Hall-Petch effect) altering the CRSS for slip and twinning [2]. Although, the CRSS for twinning can be obtained in several methods [24, 72, 73], here, the higher shear stress for twinning can promote twin nucleation and growth, and the shear stresses required to activate deformation twins include the stresses that activate the source of Frank-Read dislocation and the separation of partial dislocation to form a stacking fault [24]. On the

other hand, these stacking faults can be regarded as nano-twins of one atomic layer thickness. These nano-twins may nucleate at stacking faults in a heterogeneous or random manner and grow via Shockley partial dislocations [74]. Deformation twins are associated with the motion of Shockley partial dislocations that are side-by-side along the stacking faults in the successive $\{111\}$ -type slip planes. Thus, the CRSS for twinning can be given by the following:

$$\tau_{twinning}^{c} = \frac{\gamma_{SFE}}{b_p} + \frac{Gb_p}{d} \tag{3}$$

where $\tau_{twinning}^{c}$ is the CRSS for twinning. $b_p = \sqrt{3}b/3$ is the magnitude of the Burgers vector of Shockley partial dislocation. G=62 GPa is the shear modulus. γ_{SFE} is the SFE. It is notable that the higher γ_{SFE} and smaller grain size make twin nucleation and growth more difficult, which is a crucial factor why significant lamellar twins can be observed in the fine grains but not in the ultrafine grains in **Fig. 9**.

Meanwhile, the CRSS for slip can be calculated by the following [74]:

$$\tau_{slip}^{c} = \frac{\sigma_{YS}^{0}}{M} \tag{4}$$

where τ_{slip}^{c} is the CRSS for slip. M is the Taylor orientation factor. σ_{YS}^{0} is the yield strength of single crystal, which can be estimated by the equation [51, 74]:

$$\sigma_{YS}^{0} = \sigma_{YS} - \frac{K_{HP}}{\sqrt{d}} \tag{5}$$

where σ_{YS} is the polycrystalline yield stress that is usually obtained directly by mechanical experiments. K_{HP} is the Hall-Petch slope and d is the grain size. Meanwhile, **Fig. 14**(a) shows the distribution of Schmid factors at different strains calculated based on the EBSD data. The average Schmid factors for both dislocation slip and deformation twinning slightly decrease with increasing strain, which may be related to the grain refinement and local lattice rotation. At yielding, the average Taylor factor M=1/m_s in Eq. (4) and m_s=0.439 is considered as the average Schmid factor for slip at undeformed. Based on Eqs. (3) and (4), the CRSS for slip and

twinning at yielding are calculated, as demonstrated in **Fig. 14**(b). Grain refinement elevates the CRSS of the polycrystals, which is consistent with previously reported results [24], such that at yielding, the CRSS for slip is significantly lower than that for twinning, and thus slip is preferentially activated, which is consistent with the experimental result in **Figs. 5** and **8** where deformation twins are not observed until ε=0.2.

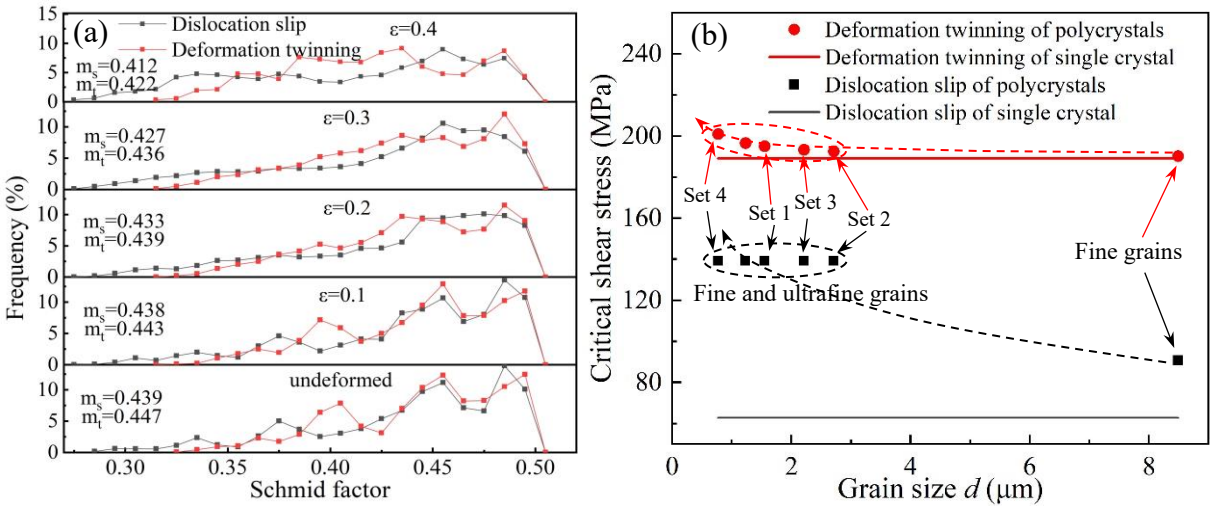

Fig. 14. (a) The distribution of Schmid factors at different strains. (b) Critical shear stresses for slip and twinning of single crystal and polycrystals at yielding.

In **Table 2**, comparing the Euler angles and maximum Schmid factors (m_s and m_t) before and after deformation of the grains in Set 1~Set 4, it can be indicated that grains do rotate during the deformation process. The rotation angles (θ) of these grains are all less than 10° when ε=0.3. It can be found that m_s is larger than m_t in grains A1-A3, and m_t is slightly larger than m_s only in the generated grain A4 in Set 1 at ε=0.3, but there is no twin in grain A4. Furthermore, only grain A3 has no change in the active slip system (S1) and twinning system (T2) before and after the deformation and has the smallest rotation angle in Set 1, 8.08°. In contrast, in grain B1, although there is no change in the active slip system (S7) and twinning system (T12), m_t increases from 0.43 at undeformed to 0.46 at ε=0.3 due to the grain B1 rotation (8.55°), whereas there is no significant change in m_s. For grains C1 and C2, m_s and m_t are the same at undeformed (0.46 and 0.44, respectively). However, m_s is greater than m_t in grain C2 at ε=0.3, while m_t is

greater than m_s in grain C1, so that grain C1 favours twinning while grain C2 may be slip-dominated under the same local stress. Meanwhile, slip makes the rotation angle of grain C2 (5.44°) smaller than that of C1 (7.74°). Thus, the twin C3 appears in grain C1. In Set 4, different grains rotate during plastic deformation. The absence of twins in grains D4, D6 and D7 with m_t larger than m_s may be due to the smaller grain size, which makes twin activation more difficult, directly suggesting that the competition between twinning and slip is related to the grain size. In addition, the active slip and twinning systems are changed only in grain D4 at ε=0.3, and grain D9 separated from grain D4 has the same active slip and twinning systems as grain D4 before deformation.

Table 2. Variation of Euler angles and the corresponding maximum Schmid factors from undeformed to ε=0.3 in **Fig. 9**. Where θ denotes the grain rotation angle. S1-S12 and T1-T12 denote 12 slip systems and 12 twin systems, respectively (details in Appendix A)

Grain set	Grain number	undeformed					ε=0.3					θ (°)
		φ_1 (°)	ϕ (°)	φ_2 (°)	m_s	m_t	φ_1 (°)	ϕ (°)	φ_2 (°)	m_s	m_t	
Set 1	A1	305.22	22.77	28.89	0.44/S4	0.42/T6	287.83	28.22	44.24	0.42/S1	0.42/T3	8.17
	A2	306.25	23.60	28.40	0.44/S4	0.42/T6	295.96	26.42	39.73	0.45/S1	0.38/T3	8.73
	A3	73.43	31.80	49.77	0.45/S1	0.41/T2	80.61	31.45	44.10	0.43/S1	0.39/T2	8.08
	A4						90.34	30.08	42.11	0.36/S8	0.37/T12	--
Set 2	B1	116.96	43.23	34.50	0.41/S7	0.43/T12	113.55	42.64	29.05	0.41/S7	0.46/T12	8.55
	B2						300.05	7.38	58.60	0.44/S1	0.47/T2	Twin
Set 3	C1	293.60	13.26	29.79	0.46/S4	0.46/T6	284.91	19.11	36.38	0.41/S4	0.42/T6	7.74
	C2	30.21	10.06	32.76	0.44/S12	0.44/T5	25.01	8.81	35.22	0.44/S12	0.43/T5	5.44
	C3						190.61	43.02	84.21	0.43/S10	0.48/T8	Twin
Set 4	D1	210.59	16.62	68.27	0.48/S10	0.42/T9	207.85	14.54	70.65	0.48/S10	0.43/T9	4.82
	D2	37.65	31.60	23.92	0.46/S12	0.45/T7	46.65	32.81	14.81	0.49/S12	0.47/T7	9.71
	D3	207.95	17.02	70.51	0.48/S10	0.41/T9	193.01	14.32	86.95	0.48/S10	0.42/T9	2.89
	D4	289.83	48.37	49.12	0.36/S1	0.40/T3	289.33	46.05	43.22	0.36/S4	0.39/T6	4.19
	D5	204.01	17.06	74.79	0.48/S10	0.41/T9	201.92	15.40	73.62	0.47/S10	0.41/T9	6.72
	D6	249.87	6.37	87.79	0.49/S1	0.50/T2	267.53	8.48	69.31	0.49/S1	0.50/T2	5.77
	D7	38.58	42.52	67.41	0.46/S1	0.49/T2	31.75	44.73	77.64	0.44/S1	0.50/T2	9.44
	D8	119.33	33.99	36.98	0.42/S10	0.38/T9	115.87	31.07	40.68	0.44/S10	0.39/T9	5.61
	D9						287.53	42.33	45.36	0.36/S1	0.37/T3	--

To further investigate the activation of slip and twinning, the resolved shear stresses for slip and twinning are calculated at yielding and ε=0.1, and the results are displayed in **Fig. 15**,

where only slip is activated at yielding due to the resolved shear stress for twinning being less than $\tau^c_{twinning}$. τ^c_{slip} and $\tau^c_{twinning}$ are calculated based on the average grain size of the material. At ε=0.1, the resolved shear stresses for twinning of grains B1 and C1 are greater than those of slip and they also exceed $\tau^c_{twinning}$, resulting in the twin activation, which is confirmed by the subsequent results based on the EBSD-IPFs and BF-TEM images. Whereas in grains D4, D6 and D7 although the resolved shear stresses for twinning is greater than the slip one, the enhanced back stress due to dislocations pile-up results in weakening the interaction of Shockley partial dislocations, which affects the expansion of the stacking faults. Furthermore, the LCs observed in HRTEM images also inhibit the development of stacking faults into twins, so that no visible lamellar twins are observed in the ultrafine grains, only nano-twins.

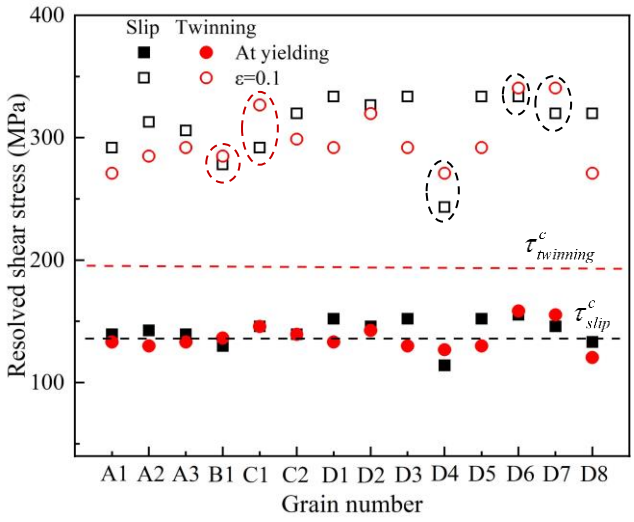

Fig. 15. The resolved shear stresses for slip and twinning of grains A1~D8 at yielding and ε=0.1.

Grain refinement has been reported to retard mechanical twinning by increasing the CRSS for twinning in TWIP steels [24]. Microscopically, the competition between twinning and dislocation slip is also affected by grain orientation and local stress. Therefore, to elucidate the effect of grain orientation on slip and twinning, IPFs of Set 1~Set 4 at different strains are shown in **Fig. 16**. It can be determined that the plastic deformation of the main three grains of Set 1 in **Fig. 16**(a) is dominated by dislocation slip, and the dispersion of grain orientation in IPFs with

increasing strain suggests that the accumulation of dislocations promotes the lattice rotation to regulate the strain distribution in the grains and further coordinate intergranular strains and stresses. In contrast, Set 2 in **Fig. 16**(b) mainly generates deformation twins to release local stresses, and the twinned matrix grain B1 is orientated close to <111>//TA direction, as reported earlier [2, 24]. A slightly dispersed distribution of grain orientation is also exhibited, which may be attributed to the accumulation of GNDs. In **Fig. 16**(c), twin C3 appears in grain C1, while dislocation slip is dominant in grain C2. Also, different modes are activated for grains with different orientations in Set 1~Set 3. However, in **Fig. 16**(d), for the grains in Set 4, even close to the <111> direction, no obvious deformation twins are produced, which may be due to the grain size regulating the activation of the deformation modes and influencing the subsequent interactions between the dislocation substructures and the stacking fault substructures. Indeed, the nano-twins are present in the ultrafine grains at larger strains in the HRTEM images.

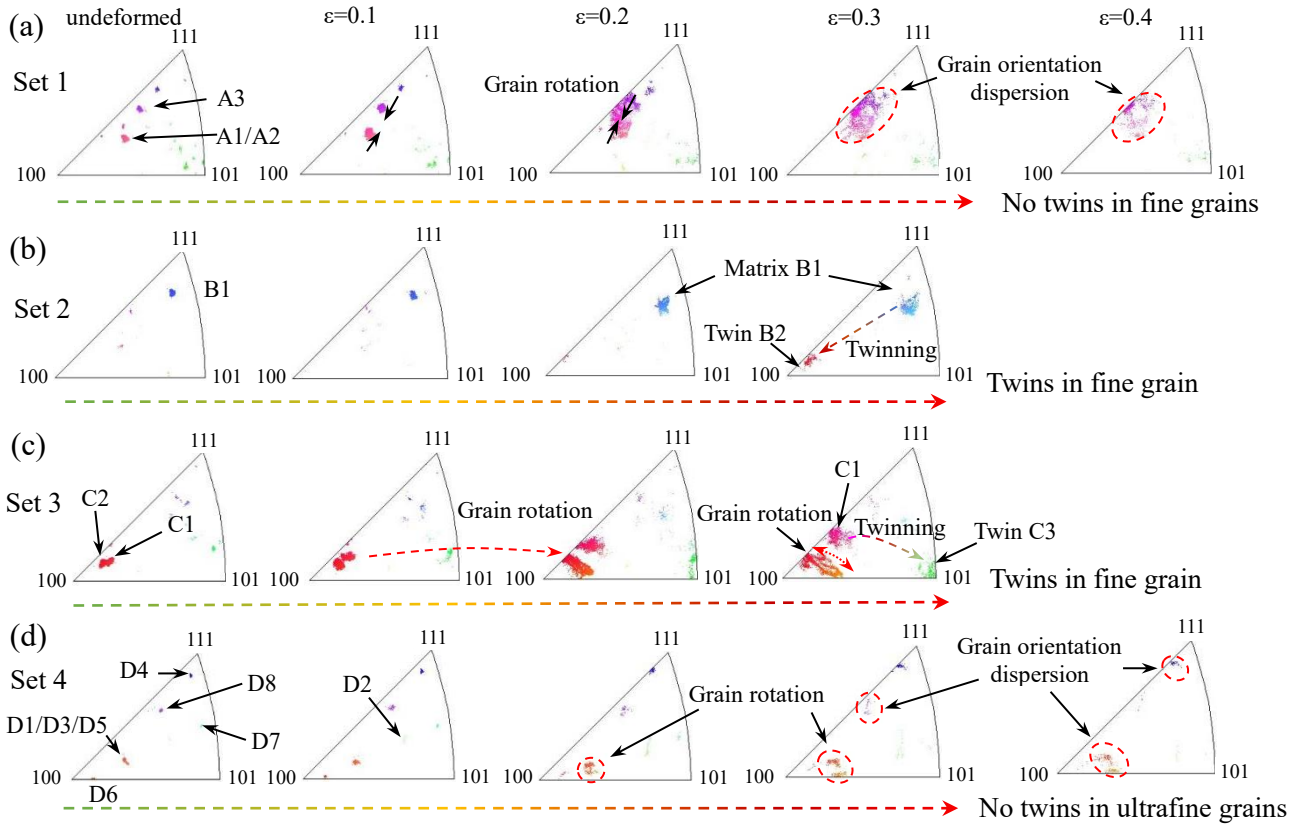

Fig. 16. Grain orientation of (a) Set 1, (b) Set 2, (c) Set 3 and (d) Set 4 along the RD//TA direction at different strains.

It is well-known that grain orientation is crucial for the activation of the deformation mechanism [1, 2]. The grain orientation dependence of dislocations and stacking fault was analysed in many reports [2, 24, 75]. The relationship between grain orientation and the Schmid factor for leading (m_{LP}) and trailing (m_{TP}) partial dislocations is displayed in **Fig. 17**(a), which suggests that the formation of stacking fault is favoured when the Schmid factor for the leading partial dislocations (m_{LP}) is larger than that of trailing partial dislocation (m_{TP}) [2, 75]. Meanwhile, a comparison of the Schmid factors for twinning (m_t) and perfect dislocation slip (m_s) in **Fig. 17**(b) reveals that $m_t > m_s$ in grain orientations close to the <111> and <101> directions, which favours the activation of twinning, as confirmed by the experimental results in **Fig. 16**. Based on **Fig. 17**(a) and (b), **Fig. 17**(c) can be obtained, and the preferred activation mechanism in different grain orientations is revealed by comparing the Schmid factors in the IPFs, where the orientation domains of $m_{LP} > m_s$ imply that the twins are easily activated, whereas slip is more preferred to dominate in orientation domains of $m_{TP} > m_{LP}$.

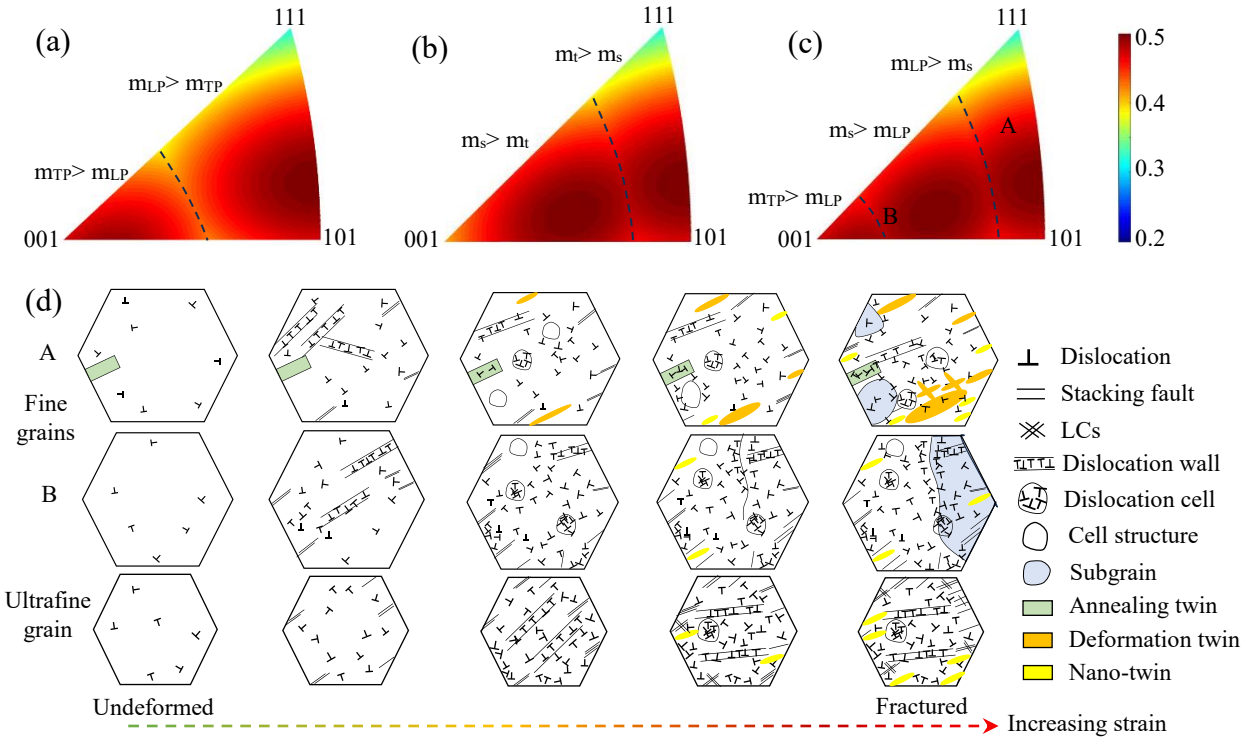

Fig. 17. Distribution of Schmid factors affected by grain orientation in IPFs for (a) leading (m_{LP}) and trailing (m_{TP}) partial dislocations, (b) perfect dislocation slip (m_s) and twinning

(m_t), and (c) m_{LP}, m_s and m_{TP}. (d) Deformation mechanisms of different grains in fine-/ultrafine-grained specimens. Where A and B denote fine grains of different grain orientation types in (c).

Nevertheless, dislocations and dislocation substructures dominate plasticity in $m_s>m_{LP}$ and $m_{TP}>m_{LP}$ types oriented grains [2]. Therefore, based on the plastic deformation of the fine-/ultrafine-grained specimens, fine grains A ($m_t>m_s$) and B ($m_s>m_t$) and ultrafine grain are selected to explore the microstructural evolution from initial deformation to fracture, respectively, as shown in **Fig. 17**(d). At initial deformation, the fine grains are predominantly dislocation-activated to form several dislocation substructures while the ultrafine grain appears clear stacking faults. With the increase of strain, the twins and dislocation cells in grain A are activated while dislocation slip dominates plasticity in grain B to successively form dislocation walls, dislocation cells and a few nano-twins. Meanwhile, the ordered arrangement of GNDs in grain B similar to grain C2 in **Fig. 9**(c) promotes the formation of new boundaries, resulting in the generation of subgrains. Grain A illustrates secondary twins and the interaction with primary twins with increasing strain. In ultrafine grains, there are fewer dislocation cells, but special LCs are formed by the interaction of stacking faults, while the overlapping of stacking faults near GBs generates nano-twins, which may be an essential factor for enhancing strain hardening in fine-/ultrafine-grained TWIP steels.

Based on the above analysis, the plastic deformation of the TWIP steels is not only affected by grain size, but also by grain orientation and local stress. Grain refinement can increase the CRSS for slip and twinning. Meanwhile, multiple mechanisms often interact and contribute to strain hardening, and induce abundant microstructures associated with dislocations and stacking faults, such as dislocation cells, dislocation walls, cell structures, stacking faults, nano-twins, laminar twins and their intertwining, resulting in synergistic effects on the strength and plasticity of the fine-/ultrafine-grained TWIP steels.

6. Conclusions

In this work, the intrinsic co-relation between microstructure and mechanical behaviour of fine-/ultrafine-grained TWIP steels was explored by utilizing the in-situ EBSD uniaxial tensile tests and TEM characterisation of the interrupted strain specimens. The activation and evolution of dislocations, stacking faults and their associated substructures were analysed by combining IPFs, PFs, BF-TEM and HRTEM images. The underlying deformation mechanisms of fine and ultrafine grains affected by grain size and grain orientation were elucidated. The main findings are summarized as follows:

(1) The fine-/ultrafine-grained TWIP steels were prepared by rolling and stress-relief annealing. Their higher strain hardening rates and excellent mechanical properties with the PSE increasing to ~71 GPa·% are attributed to the abundant microstructures and their interactions in fine and ultrafine grains during plastic deformation, including dislocations and associated dislocation cells, dislocation walls and dislocation tangles, stacking faults and associated LCs, nano-twins, and the intertwining of primary and secondary twins.

(2) The increase in GND density can be well estimated by the modified Ashby′s model. The GND density is lower in grains with twin-mediated plasticity compared to grains with slip-dominated plasticity. The higher GND density favours local lattice rotation, which can facilitate the generation of subgrains and new boundaries. This directly results in an increase in LAGBs frequency and a decrease in deformation twin boundary fraction during deformation. Meanwhile, the generated boundaries including subgrain boundaries and twin boundaries can promote grain refinement to reduce the MFP of dislocations, thus enhancing strain hardening.

(3) TEM characterisation reveals that dislocation is preferentially activated and subsequently dominates plasticity in fine grains while stacking fault is more pronounced in ultrafine grains during the initial deformation. With increasing strain, some obvious laminar primary and secondary twins are generated in fine grains, which are intertwined with each other,

while obvious LCs are found in the ultrafine grains, and nano-twins are formed by the overlapping of stacking faults at higher strains, which can further enhance strain hardening.

(4) The competition and synergy between dislocation slip and deformation twinning are not only affected by grain orientation, but also controlled by the grain size and local stress. By comparing the distribution of Schmid factors for leading and trailing partial dislocations, perfect dislocation slip and twinning in IPFs, it is elucidated that the <111> and <101> directions are favourable for twinning while <001> direction is beneficial for slip. Furthermore, the resolved shear stresses for slip and twinning are calculated based on Schmid factors, suggesting that twinning is strongly inhibited in ultrafine grains. Also, the microstructural evolution reveals more stacking faults and nano-twins, but fewer dislocation cells in ultrafine grains.

CRediT authorship contribution statement

Wang Cai: Conceptualization, Data curation, Methodology, Software, Investigation, Visualization, Writing-review & editing. **Chaoyang Sun**: Funding acquisition, Methodology, Resources, Supervision, Project administration, Writing-review & editing. **Hongjia Zhang**: Funding acquisition, Methodology, Investigation, Data curation & editing. **Chunhui Wang**: Methodology, Writing-review & editing. **Linghui Meng**: Software, Writing-review & editing. **M.W. Fu**: Funding acquisition, Methodology, Supervision, Writing-review & editing.

Declaration of competing interest

The authors declare that they do not have any commercial interests or personal relationships that could have appeared to influence the work reported in this paper.

Data availability statement

The raw/processed data required to reproduce these findings cannot be shared at this time as the data also forms part of an ongoing study.

Acknowledgements

The authors acknowledge the funding supported by the National Natural Science Foundation of China (No. 52175285, 52161145407, U22A20186, 52001325, 51835011), and the projects of G-SB4Y, 1-ZE1W and 1-WZ4W from the Hong Kong Polytechnic University.

Appendix A: The slip and twin systems of TWIP steels with fine and ultrafine grains

Table A1. The main slip systems of TWIP steel in this work.

No.	Slip plane	Slip direction	No.	Slip plane	Slip direction
S1	(1 1 1)	[-1 1 0]	S7	(1 -1 1)	[1 0 -1]
S2	(1 1 1)	[1 0 -1]	S8	(1 -1 1)	[0 1 1]
S3	(1 1 1)	[0 -1 1]	S9	(1 -1 1)	[1 1 0]
S4	(-1 1 1)	[1 0 1]	S10	(1 1 -1)	[-1 1 0]
S5	(-1 1 1)	[1 1 0]	S11	(1 1 -1)	[1 0 1]
S6	(-1 1 1)	[0 -1 1]	S12	(1 1 -1)	[0 1 1]

Table A2. The main twin systems of TWIP steel in this work.

No.	Twin plane	Twin direction	No.	Twin plane	Twin direction
T1	(1 1 1)	[1 1 -2]	T7	(-1 -1 1)	[1 1 2]
T2	(1 1 1)	[-2 1 1]	T8	(-1 -1 1)	[2 -1 1]
T3	(1 1 1)	[1 -2 1]	T9	(-1 -1 1)	[-1 2 1]
T4	(-1 1 1)	[2 1 1]	T10	(1 -1 1)	[1 2 1]
T5	(-1 1 1)	[1 2 -1]	T11	(1 -1 1)	[2 1 -1]
T6	(-1 1 1)	[1 -1 2]	T12	(1 -1 1)	[-1 1 2]

References

[1] B.C. De Cooman, Y. Estrin, S.K. Kim, Twinning-induced plasticity (TWIP) steels, Acta Mater. 142 (2018) 283-362.

[2] J. Punyafu, S. Hwang, S. Ihara, H. Saito, N. Tsuji, M. Murayama, Microstructural factors dictating the initial plastic deformation behavior of an ultrafine-grained Fe–22Mn-0.6C TWIP steel, Mater. Sci. Eng. A 862 (2023) 144506.

[3] F. Berrenberg, C. Haase, L.A. Barrales-Mora, D.A. Molodov, Enhancement of the strength-ductility combination of twinning-induced/transformation-induced plasticity steels by reversion annealing, Mater. Sci. Eng. A 681 (2017) 56-64.

[4] S. Picak, T. Wegener, S.V. Sajadifar, C. Sobrero, J. Richter, H. Kim, T. Niendorf, I. Karaman, On the low-cycle fatigue response of CoCrNiFeMn high entropy alloy with

ultra-fine grain structure, Acta Mater. 205 (2021) 116540.
[5] I.B. Timokhina, A. Medvedev, R. Lapovok, Severe plastic deformation of a TWIP steel, Mater. Sci. Eng. A 593 (2014) 163-169.
[6] Y.W. Tham, M.W. Fu, H.H. Hng, Q.X. Pei, K.B. Lim, Microstructure and properties of Al-6061 alloy by equal channel angular extrusion for 16 passes, Mater. Manuf. Processes 22(7-8) (2007) 819-824.
[7] S. Shahrezaei, Y. Sun, S.N. Mathaudhu, Strength-ductility modulation via surface severe plastic deformation and annealing, Mater. Sci. Eng. A 761 (2019) 138023.
[8] J.G. Kim, N.A. Enikeev, M.M. Abramova, B.H. Park, R.Z. Valiev, H.S. Kim, Effect of initial grain size on the microstructure and mechanical properties of high-pressure torsion processed twinning-induced plasticity steels, Mater. Sci. Eng. A 682 (2017) 164-167.
[9] N. Tsuji, Y. Saito, H. Utsunomiya, S. Tanigawa, Ultra-fine grained bulk steel produced by accumulative roll-bonding (ARB) process, Scripta Mater. 40(7) (1999) 795-800.
[10] M. Seleznev, N. Kaden, C. Renzing, M. Schmidtchen, U. Prahl, H. Biermann, A. Weidner, Microstructural evolution of the bonding zone in TRIP-TWIP laminate produced by accumulative roll bonding, Mater. Sci. Eng. A 840 (2022) 142866.
[11] C. Lei, X. Deng, X. Li, Z. Wang, Simultaneous enhancement of strength and ductility through coordination deformation and multi-stage transformation induced plasticity (TRIP) effect in heterogeneous metastable austenitic steel, Scripta Mater. 162 (2019) 421-425.
[12] Y. Wei, F. Zhan, Z. Li, Y. Shi, M. Zhu, Y. Zheng, J. Sheng, P. La, Superior strength and ductility of 316L stainless steel induced by micro/nano/ultrafine-grains multiphase complex structures, Mater. Sci. Eng. A 859 (2022) 144194.
[13] B. Gao, Q. Lai, Y. Cao, R. Hu, L. Xiao, Z. Pan, N. Liang, Y. Li, G. Sha, M. Liu, Ultrastrong low-carbon nanosteel produced by heterostructure and interstitial mediated warm rolling, Sci. Adv. 6(39) (2020) eaba8169.
[14] C.Y. Hung, Y. Bai, N. Tsuji, M. Murayama, Grain size altering yielding mechanisms in ultrafine grained high-Mn austenitic steel: Advanced TEM investigations, J. Mater. Sci. Technol. 86 (2021) 192-203.
[15] J. Y. Lee, J. S. Hong, S. H. Kang, Y. K. Lee, The effect of austenite grain size on deformation mechanism of Fe–17Mn steel, Mater. Sci. Eng. A 809 (2021) 140972.
[16] D.M. Xu, G.Q. Li, X.L. Wan, R.L. Xiong, G. Xu, K.M. Wu, M.C. Somani, R.D.K. Misra, Deformation behavior of high yield strength – High ductility ultrafine-grained 316LN austenitic stainless steel, Mater. Sci. Eng. A 688 (2017) 407-415.
[17] S. Curtze, V.T. Kuokkala, Dependence of tensile deformation behavior of TWIP steels on stacking fault energy, temperature and strain rate, Acta Mater. 58(15) (2010) 5129-5141.
[18] M. Liu, J.Y. Lin, S. Nambu, P. Wang, H.L. Chen, S.E. Shin, L. Zhang, T. Koseki, Investigation of work hardening behavior in multilayered steels architected by twinning induced plasticity steel and martensitic steel during uniaxial tension, Mater. Sci. Eng. A 811 (2021) 140996.
[19] I.C. Jung, B.C. De Cooman, Temperature dependence of the flow stress of Fe–18Mn–0.6C–xAl twinning-induced plasticity steel, Acta Mater. 61(18) (2013) 6724-6735.
[20] O. Bouaziz, N. Guelton, Modelling of TWIP effect on work-hardening, Mater. Sci. Eng. A

319-321 (2001) 246-249.
[21] I. Gutierrez-Urrutia, D. Raabe, Multistage strain hardening through dislocation substructure and twinning in a high strength and ductile weight-reduced Fe–Mn–Al–C steel, Acta Mater. 60(16) (2012) 5791-5802.
[22] H. Zhi, C. Zhang, S. Antonov, H. Yu, T. Guo, Y. Su, Investigations of dislocation-type evolution and strain hardening during mechanical twinning in Fe-22Mn-0.6C twinning-induced plasticity steel, Acta Mater. 195 (2020) 371-382.
[23] N. Hansen, Hall–Petch relation and boundary strengthening, Scripta Mater. 51(8) (2004) 801-806.
[24] I. Gutierrez-Urrutia, S. Zaefferer, D. Raabe, The effect of grain size and grain orientation on deformation twinning in a Fe–22wt.% Mn–0.6wt.% C TWIP steel, Mater. Sci. Eng. A 527(15) (2010) 3552-3560.
[25] D.T. Pierce, J.A. Jiménez, J. Bentley, D. Raabe, C. Oskay, J.E. Wittig, The influence of manganese content on the stacking fault and austenite/ε-martensite interfacial energies in Fe–Mn–(Al–Si) steels investigated by experiment and theory, Acta Mater. 68 (2014) 238-253.
[26] A. Saeed-Akbari, A. Schwedt, W. Bleck, Low stacking fault energy steels in the context of manganese-rich iron-based alloys, Scripta Mater. 66(12) (2012) 1024-1029.
[27] S. Sun, M. Cai, H. Ding, H. Huang, H. Pan, Deformation mechanisms of a novel Mn-based 1 GPa TRIP/TWIP assisted lightweight steel with 63% ductility, Mater. Sci. Eng. A 802 (2021) 140658.
[28] R. Mohammadzadeh, M. Mohammadzadeh, Inverse grain size effect on twinning in nanocrystalline TWIP steel, Mater. Sci. Eng. A 747 (2019) 265-275.
[29] R. Ueji, N. Tsuchida, D. Terada, N. Tsuji, Y. Tanaka, A. Takemura, K. Kunishige, Tensile properties and twinning behavior of high manganese austenitic steel with fine-grained structure, Scripta Mater. 59(9) (2008) 963-966.
[30] Y. Bai, H. Kitamura, S. Gao, Y. Tian, N. Park, M.H. Park, H. Adachi, A. Shibata, M. Sato, M. Murayama, N. Tsuji, Unique transition of yielding mechanism and unexpected activation of deformation twinning in ultrafine grained Fe-31Mn-3Al-3Si alloy, Sci. Rep. 11(1) (2021) 15870.
[31] J. Gao, S. Jiang, H. Zhao, Y. Huang, H. Zhang, S. Wang, G. Wu, Y. Wu, H. Wu, A. Davydov, W.M. Rainforth, Z. Lu, X. Mao, Enhancing strength and ductility in a near medium Mn austenitic steel via multiple deformation mechanisms through nanoprecipitation, Acta Mater. 243(2023) 118538.
[32] J. Li, C. Ding, W. Chen, D. Shan, B. Guo, J. Xu, Strain localization and ductile fracture mechanism of micro/mesoscale deformation in ultrafine-grained pure copper, Mater. Design 229 (2023) 111873.
[33] S. Kang, J.G. Jung, M. Kang, W. Woo, Y.K. Lee, The effects of grain size on yielding, strain hardening, and mechanical twinning in Fe–18Mn–0.6C–1.5Al twinning-induced plasticity steel, Mater. Sci. Eng. A 652 (2016) 212-220.
[34] H. Zhi, S. Antonov, C. Zhang, Z. Guo, Y. Su, Origins of back stress strengthening in Fe-22Mn-0.6C (-3Al) TWIP steels, Mater. Sci. Eng. A 792 (2020) 139834.

[35] Y.K. Lee, Microstructural evolution during plastic deformation of twinning-induced plasticity steels, Scripta Mater. 66(12) (2012) 1002-1006.
[36] X. Fu, X. Wu, Q. Yu, Dislocation plasticity reigns in a traditional twinning-induced plasticity steel by in situ observation, Mater. Today Nano 3 (2018) 48-53.
[37] Y.T. Zhu, X.Z. Liao, X.L. Wu, Deformation twinning in nanocrystalline materials, Prog. Mater. Sci. 57(1) (2012) 1-62.
[38] P. Chen, S.C. Mao, Y. Liu, F. Wang, Y.F. Zhang, Z. Zhang, X.D. Han, In-situ EBSD study of the active slip systems and lattice rotation behavior of surface grains in aluminum alloy during tensile deformation, Mater. Sci. Eng. A 580 (2013) 114-124.
[39] S. Wei, G. Zhu, C.C. Tasan, Slip-twinning interdependent activation across phase boundaries: An in-situ investigation of a Ti-Al-V-Fe (α+β) alloy, Acta Mater. 206 (2021) 116520.
[40] C. Wang, W. Cai, C. Sun, X. Li, L. Qian, J. Jiang, Strain rate effects on mechanical behavior and microstructure evolution with the sequential strains of TWIP steel, Mater. Sci. Eng. A 835 (2022) 142673.
[41] Kim, J. K., Kwon, M. H., De Cooman, B. C. On the deformation twinning mechanisms in twinning-induced plasticity steel. Acta Mater. 141 (2017) 444-455.
[42] N. Tsuji, S. Ogata, H. Inui, I. Tanaka, K. Kishida, S. Gao, W. Mao, Y. Bai, R. Zheng, J.P. Du, Strategy for managing both high strength and large ductility in structural materials–sequential nucleation of different deformation modes based on a concept of plaston, Scripta Mater. 181 (2020) 35-42.
[43] D.M. Xu, X.L. Wan, J.X. Yu, G. Xu, G.Q. Li, Effect of grain refinement on strain hardening and fracture in austenitic stainless steel, Mater. Sci. Technol. 34(11) (2018) 1344-1352.
[44] G. Niu, H. Wu, D. Zhang, N. Gong, D. Tang, Heterogeneous nano/ultrafine-grained medium Mn austenitic stainless steel with high strength and ductility, Mater. Sci. Eng. A 725 (2018) 187-195.
[45] Y.Z. Tian, Y. Bai, L.J. Zhao, S. Gao, H.K. Yang, A. Shibata, Z.F. Zhang, N. Tsuji, A novel ultrafine-grained Fe 22Mn 0.6C TWIP steel with superior strength and ductility, Mater. Charact. 126 (2017) 74-80.
[46] R. Kalsar, S. Suwas, A novel way to enhance the strength of twinning induced plasticity (TWIP) steels, Scripta Mater.154 (2018) 207-211.
[47] Y.Z. Tian, Y. Bai, M.C. Chen, A. Shibata, D. Terada, N. Tsuji, Enhanced Strength and Ductility in an Ultrafine-Grained Fe-22Mn-0.6C Austenitic Steel Having Fully Recrystallized Structure, Metall. Mater. Trans. A 45(12) (2014) 5300-5304.
[48] J. Zhang, Y. Xu, Y. Wang, S. Wang, Achieving heterogeneous TWIP/TRIP steel with 1GPa strength and 72% ductility by introducing austenite + martensite lamella structure, Mater. Charact.197 (2023) 112709.
[49] Zhu, C., Harrington, T., Gray III, G. T., Vecchio, K. S. Dislocation-type evolution in quasi-statically compressed polycrystalline nickel. Acta Mater. 155 (2018) 104-116.
[50] C. Du, Y. Gao, M. Zha, C. Wang, H. Jia, H.-Y. Wang, Deformation-induced grain rotation and grain boundary formation achieved through dislocation-disclination reactions in polycrystalline hexagonal close-packed metals, Acta Mater. 250 (2023) 118855.

[51] W. Cai, C. Wang, C. Sun, L. Qian, M.W. Fu, Microstructure evolution and fracture behaviour of TWIP steel under dynamic loading, Mater. Sci. Eng. A 851 (2022) 143657.
[52] Y. Zou, H. Ding, Y. Zhang, Z. Tang, Microstructural evolution and strain hardening behavior of a novel two-stage warm rolled ultra-high strength medium Mn steel with heterogeneous structures, Int. J. Plast. 151 (2022) 103212.
[53] Y. Qiao, Y. Chen, F.H. Cao, H.Y. Wang, L.H. Dai, Dynamic behavior of CrMnFeCoNi high-entropy alloy in impact tension, Int. J. Impact Eng. 158 (2021) 104008.
[54] Q. Liu, L. Fang, Z. Xiong, J. Yang, Y. Tan, Y. Liu, Y. Zhang, Q. Tan, C. Hao, L. Cao, J. Li, Z. Gao, The response of dislocations, low angle grain boundaries and high angle grain boundaries at high strain rates, Mater. Sci. Eng. A 822 (2021) 141704.
[55] Y. Cao, S. Ni, X. Liao, M. Song, Y. Zhu, Structural evolutions of metallic materials processed by severe plastic deformation, Mater. Sci. Eng. R 133 (2018) 1-59.
[56] Y.Q. Ning, T. Wang, M.W. Fu, M.Z. Li, L. Wang, C.D. Zhao, Competition between work-hardening effect and dynamic-softening behavior for processing as-cast GH4720Li superalloys with original dendrite microstructure during moderate-speed hot compression, Mater. Sci. Eng. A 642 (2015) 187-193.
[57] J. Park, M. Kang, S.S. Sohn, S. H. Kim, H.S. Kim, N.J. Kim, S. Lee, Quasi-static and dynamic deformation mechanisms interpreted by microstructural evolution in TWinning Induced Plasticity (TWIP) steel, Mater. Sci. Eng. A 684 (2017) 54-63.
[58] Yang, M., Pan, Y., Yuan, F., Zhu, Y., Wu, X. Back stress strengthening and strain hardening in gradient structure. Mater. Res. Lett. 4(3) (2016) 145-151.
[59] J. Li, M. Yi, H. Wu, Q. Fang, Y. Liu, B. Liu, K. Zhou, P.K. Liaw, Fine-grain-embedded dislocation-cell structures for high strength and ductility in additively manufactured steels, Mater. Sci. Eng. A 790 (2020) 139736.
[60] A. Mishra, B. Kad, F. Gregori, M. Meyers, Microstructural evolution in copper subjected to severe plastic deformation: Experiments and analysis, Acta Mater. 55(1) (2007) 13-28.
[61] Y.W. Tham, M.W. Fu, H.H. Hng, M.S. Yong, K.B. Lim, Bulk nanostructured processing of aluminum alloy, J. Mater. Process. Tech. 192-193 (2007) 575-581.
[62] X. Wu, P. Jiang, L. Chen, F. Yuan, Y.T. Zhu, Extraordinary strain hardening by gradient structure, P. Natl. Acad. Sci. USA 111(20) (2014) 7197-7201.
[63] M. Ashby, The deformation of plastically non-homogeneous materials, Philos. Mag. 21(170) (1970) 399-424.
[64] J. Gao, Y. Huang, D. Guan, A.J. Knowles, L. Ma, D. Dye, W.M. Rainforth, Deformation mechanisms in a metastable beta titanium twinning induced plasticity alloy with high yield strength and high strain hardening rate, Acta Mater. 152 (2018) 301-314.
[65] J.K. Kim, In-situ TEM investigation of deformation mechanisms of twinning-induced plasticity steel, Mater. Charact. 196 (2023) 112583.
[66] X. Wu, Y. Zhu, Heterogeneous materials: a new class of materials with unprecedented mechanical properties, Mater. Res. Lett. 5(8) (2017) 527-532.
[67] P. Pandey, M. Heczko, N. Khatavkar, N. Mazumder, A. Sharma, A. Singh, M.J. Mills, K. Chattopadhyay, On the faulting and twinning mediated strengthening and plasticity in a γ′ strengthened CoNi-based superalloy at room temperature, Acta Mater. 252 (2023) 118928.

[68] Y. Chong, R. Gholizadeh, T. Tsuru, R. Zhang, K. Inoue, W. Gao, A. Godfrey, M. Mitsuhara, J.W. Morris, Jr., A.M. Minor, N. Tsuji, Grain refinement in titanium prevents low temperature oxygen embrittlement, Nat. Commun. 14(1) (2023) 404.
[69] J. Wang, J. Zou, H. Yang, H. Huang, Z. Liu, S. Ji, Strength improvement of CoCrNi medium-entropy alloy through introducing lattice defects in refined grains, Mater. Charact. 193 (2022) 112254.
[70] N.K. Tewary, S.K. Ghosh, S. Chatterjee, A. Ghosh, Deformation and annealing behaviour of dual phase TWIP steel from the perspective of residual stress, faults, microstructures and mechanical properties, Mater. Sci. Eng. A 733 (2018) 43-58.
[71] S. Gustafson, W. Ludwig, P. Shade, D. Naragani, D. Pagan, P. Cook, C. Yildirim, C. Detlefs, M.D. Sangid, Quantifying microscale drivers for fatigue failure via coupled synchrotron X-ray characterization and simulations, Nat. Commun. 11(1) (2020) 3189.
[72] D.R. Steinmetz, T. Jäpel, B. Wietbrock, P. Eisenlohr, I. Gutierrez-Urrutia, A. Saeed-Akbari, T. Hickel, F. Roters, D. Raabe, Revealing the strain-hardening behavior of twinning-induced plasticity steels: Theory, simulations, experiments, Acta Mater. 61(2) (2013) 494-510.
[73] Y.F. Shen, N. Jia, Y.D. Wang, X. Sun, L. Zuo, D. Raabe, Suppression of twinning and phase transformation in an ultrafine grained 2 GPa strong metastable austenitic steel: Experiment and simulation, Acta Mater. 97 (2015) 305-315.
[74] K. Li, B. Yu, R.D.K. Misra, G. Han, Y.T. Tsai, C.W. Shao, C.J. Shang, J.R. Yang, Z.F. Zhang, Strain rate dependence on the evolution of microstructure and deformation mechanism during nanoscale deformation in low carbon-high Mn TWIP steel, Mater. Sci. Eng. A 742 (2019) 116-123.
[75] D. Geissler, J. Freudenberger, A. Kauffmann, M. Krautz, H. Klauss, A. Voss, J. Eickemeyer, L. Schultz, Appearance of dislocation-mediated and twinning-induced plasticity in an engineering-grade FeMnNiCr alloy, Acta Mater. 59(20) (2011) 7711-7723.